School of Mathematical, Physical
and Computational Sciences

University of Reading

Department of Mathematics and Statistics

Preprint MPCS-2017-08

26 February 2018

Capillary transport in particulate porous materials at low levels of saturation: the mathematical model and a comparison with experimental observations

by

Alex V. Lukyanov, Vladimir Mitkin, Theo G. Theofanous and **Mike Baines**

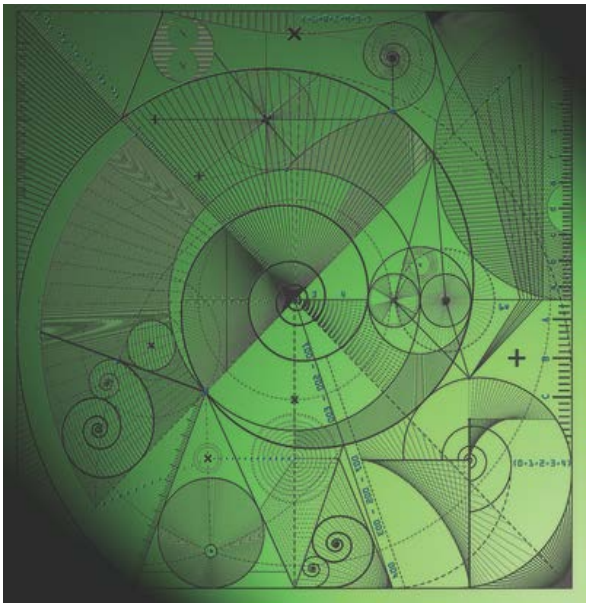

Capillary transport in particulate porous materials at low levels of saturation: the mathematical model and a comparison with experimental observations.

Alex V. Lukyanov[†], Vladimir Mitkin[‡], Theo G. Theofanous[§] and Mike Baines[†]
[†] *School of Mathematical and Physical Sciences, University of Reading, Reading, RG6 6AX, UK*
[‡] *Aerospace Research Laboratory, University of Virginia, Charlottesville, VA 22903, USA and*
[§] *University of California, Santa Barbara, CA 93106, USA*

We have established previously, in a pilot study, that the spreading of liquids in granular porous materials at low levels of saturation, typically less than 10% of the available void space, has very distinctive features in comparison to that at higher saturation levels. In particular, it has been shown, on theoretical grounds, that the spreading is controlled by a special type of diffusional process, that its physics can be captured by an equation of the super-fast diffusion class, and that these findings were supported by first-of-a-kind experiments. In this paper, we take these findings to the next level including deeper examination and exposition of the theory, an expanded set of experiments to address scaling properties, and systematic evaluations of the predictive performance against these experimental data, keeping in mind also potential practical applications.

I. INTRODUCTION

Even a small amount of a liquid added to a dry granular material may dramatically change its structural properties due to the appearance of a strong capillary cohesion force between the particles [1–4]. The strong capillary force, of the order of $F \sim 2\pi R\gamma\cos\theta_c$, is due to the liquid bridges (pendular rings) formed at the point of particle contact [5, 6]. Here, R is the average particle radius, γ is the surface tension coefficient and θ_c is the static contact angle of the liquid formed at the three-phase contact line on the flat surface of the solid. A simple estimate for water at room temperature ($\gamma = 72\,\mathrm{mN/m}$) and sand particles ($\theta_c = 30^\circ$) of $400\,\mu$m in diameter results in $F \approx 8\times10^{-5}\,\mathrm{N}$, which is much larger than the gravity force acting on each particle $\approx 8\times10^{-8}\,\mathrm{N}$. It is interesting to note, that the cohesive force is practically independent of the liquid content, that is the value of saturation, as far as the liquid morphology consists of isolated pendular rings.

The formation of isolated liquid bridges is the main characteristic feature of the pendular regime of wetting in porous materials, when liquid volumes inside the porous matrix are only connected via thin films developed on rough surfaces of the particles, Fig. 1. The pendular regime of wetting is observed in a range of saturations $0.2\% \le s \le 10\%$, where the saturation s is defined as the ratio of the liquid volume V_L within a sample volume element V to the available void space $s = \frac{V_L}{V_e}$ [1–3, 7].

The minimal saturation level s_0 is observed when the liquid bridges start to disappear, and when the porous network starts to lose its cohesive and transport properties. At this level of saturation, the bridges are predominantly formed between asperities on the grains, as is illustrated in Fig. 2, so that permeability of the entire porous network is greatly reduced when the saturation is approaching this critical level [1, 8]; at this point essentially the whole quantity of the liquid resides within the surface roughness of the grains. As a result, the value of s_0 can be defined by the non-dimensional parameter

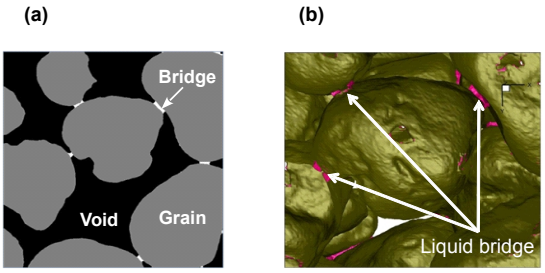

FIG. 1. Illustration of isolated bridges at low levels of saturation. (a) Micro-x-ray computer tomography (MicroXCT) image, typical from our experiments. (b) 3D image reconstruction of MicroXCT data. The liquid within the grain roughness is invisible to MicroXCT, since resolution is limited to a few micrometres.

$\frac{\delta_R}{R}$, where parameter δ_R has the dimension of length and can be interpreted as the characteristic average thickness of the surface roughness. For example, a threshold value $s_0 \approx 0.2\%$ has been observed in experiments using spherical particles, average radius $R = 187.5\,\mu$m, with the maximum surface roughness amplitude of approximately 500 nm as determined by scanning force microscopy [1]. At the same time, in our experiments with Ottawa sands, average grain radius $R \approx 250\,\mu$m with the surface roughness amplitude distributed between 250 nm and $3\,\mu$m [9], a minimal value of $s_0 \approx 0.6\%$ was observed, implying an effective δ_R value of $1.5\,\mu$m. One can see that the lower is the surface roughness on average, the lower is the critical value s_0.

If we now consider spherical (or nearly spherical) grains and take into account that only some part of the volume $4\pi R^2\delta_R$ is available for the liquid during the spreading, then the value of saturation due to the liquid distributed

on the rough surface of the grains is

$$s_0 = 3\alpha_R \frac{1-\phi}{\phi} \frac{\delta_R}{R}, \qquad (1)$$

where parameter α_R is the fraction of the surface volume occupied by the liquid and ϕ is the porosity. The value of α_R is defined by the properties of the surface roughness, and is reflected by the value of effective permeability of the surface layers [10–12].

In our experiments, as we will show, parameter α_R is found to be $\alpha_R \approx 0.2$ at equilibrium. We can thus estimate, using (1), that to get $s_0 = 0.6\%$ at $R = 250\,\mu$m and $\phi = 30\%$, one needs to have $\delta_R \approx 1\,\mu$m, while to get $s_0 = 0.2\%$ at $R = 187.5\,\mu$m and $\phi = 30\%$, one needs to have $\delta_R \approx 270\,$nm.

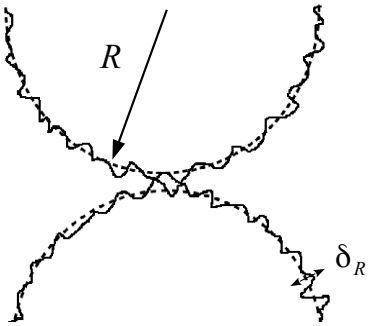

FIG. 2. The contact zone between two rough spherical particles.

Above $s_c \approx 10\%$, liquid bridges coalesce into more complex structures, like trimers and pentamers, and the pendular wetting state gradually transforms into the so called funicular regime, while the global connectivity of the liquid volumes is still absent, Fig. 3. Finally, at $s \approx 30\%$ a percolation transition occurs when the largest clusters contain about 90% of the available liquid.

Our prime concern here is liquid transport in the range of saturations corresponding to the pendular regime of wetting, which is important for accurate representation of soil-liquid characteristic curves at the lower end of saturations to study biological processes, such as plant water uptake and microbial activity, and spreading of persistent (non-volatile) liquids in arid environments and dry industrial installations [7, 12].

The peculiar character of the diffusion processes in the pendular regime of wetting, when porous network connectivity is conditioned by thin liquid films, has been recognized previously [7, 10–15]. It has been shown that specific features of liquid transport at low levels of saturation should lead to a special class of mathematical problems, when effective coefficient of non-linear diffusion $D(s)$ diverges at the lower end of saturation, that is in the limit $\lim_{s\to 0} D(s) = s^\lambda$ with $\lambda < 0$.

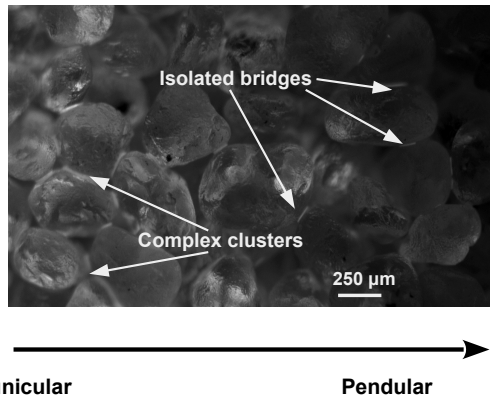

FIG. 3. An UV fluorescence image of the liquid (TEHP) distribution in sands in the transition from the pendular to the funicular regimes of wetting, at $s > 10\%$.

For the first time, the diverging behaviour of the diffusion coefficient $D(s)$, named *hyperdispersion*, was predicted in the analysis of spreading in porous networks driven by the disjoining pressure $\Pi(h)$ of nanoscale (thickness $h \sim 1 - 100\,$nm) wetting films [14, 15]. A range of admissible λ has been predicted depending on the behaviour of the disjoining pressure $\Pi(h)$ as a function of the film thickness h, including hyperdispersive exponents $\lambda < 0$. Evidence of hyperdispersive behaviour has been observed in two-phase fluid flows with the exponent $\lambda \approx -1$ [16]. On the other hand, studies of persistent liquids spreading in sands have revealed another mechanism leading to the formulation of a *superfast* non-linear diffusion model [7]. The driving force in this model is due to the macroscopic capillary pressure developed on a scale of the surface roughness δ_R with $D(s) \propto (s - s_0)^{-3/2}$, diverging at much higher values of saturation $s = s_0 \approx 0.6\%$ than that anticipated in [14, 15] and with a different exponent value $\lambda = -3/2$. A comparison between a lead-in theoretical model of superfast diffusion and experimental observations has shown very good agreement [7]. In this study, we further pursue this work, aiming for enhanced definition of the theoretical approach and a more detailed comparison with experiments, including new ones designed to explore scaling properties of the process.

II. EXPERIMENTAL OBSERVATIONS

Our experiments have been conducted, as in our previous work, by carefully placing small liquid drops of a controlled volume, $3\,\text{mm}^3 \le V_D \le 12\,\text{mm}^3$, on naturally packed sand beds (slightly shaken to level out) with porosity levels of $\phi \approx 0.3$. To obtain the desired low-dispersion samples, we processed from the standard

Ottawa Sand (EMD Chemicals, product SX0075) using a mini-sieves set (Bel-Art Products). The average radii were $R = 0.32, 0.26, 0.25, 0.2$ and $0.14\,\mathrm{mm}$ with the standard deviations, w_R, as is presented in Table I. For liquids, we have used several low-volatility (organophosphate) liquids of varying viscosity and surface tension: tributyl phosphate (TBP, molar weight $266.32\,\mathrm{g/mol}$), CAS 126-73-8; Tris(2-ethylhexyl) phosphate (TEHP, molar weight $434.63\,\mathrm{g/mol}$), CAS 78-42-2 and tricresyl phosphate (TCP, molar weight $368.37\,\mathrm{g/mol}$), CAS 1330-78-5 (Sigma-Aldrich); the details can be found in Table I. The contact angles θ_c of TBP, TEHP and TCP measured on smooth/rough flat glass surfaces in our laboratory at $20\,\mathrm{C}^\circ$ were found to be at $10^\circ/0^\circ$, $10^\circ/0^\circ$ and $30^\circ/20^\circ$ respectively.

The spreading process has been monitored by time-lapse photography using UV-excited fluorescence of the liquid obtained by adding a small amount (1% by weight) of Coumarin 503 dye. We have verified that the liquid properties were unaffected by the presence of the dye. The photographs, Fig. 4, were taken by 10.7 MPixel digital cameras (Lumenera Corporation) equipped with a macro-lens and focused to resolve individual grains. The lens was covered by long-pass glass filters to cut off scattered excitation light. No significant background signal could be detected in the absence of the dyed liquid in the range of exposures used in the experiments.

It has been demonstrated previously that after several minutes following the drop contact with the porous bed, the wet region in the sand had the shape of a hemisphere [7]. Since for this class of persistent liquids evaporation on the time scale of the experiment is practically negligible (we only observed some evaporation effects for TBP at the very late stages of spreading), this implies, first of all, that the effects of gravity play no significant role. Secondly, the externally visible wet spot diameter can be directly converted into the wet volume V. The wet volume, in turn, can be converted into average saturation $\bar{s} = \frac{V_D}{\phi V}$. Typical evolution dynamics of the wet regions obtained by depositing TCP liquid drops of different volumes ($V_D = 3, 6$ and $12\,\mathrm{mm}^3$) is shown in Fig. 5. One can see that the wet volume monotonically increases with time eventually saturating at $\bar{s} = s_f \approx s_0$, Table I, with parameter s_f apparently being independent of the amount of the liquid deposited, V_D. Theoretically, one can presume that the thin liquid film formed on the rough surfaces of the grains should be ultimately spread further out, by capillary action, forming even thinner, nano-scale ($\sim 1\,\mathrm{nm}$) liquid films, so that the observed asymptotic spreading would be in fact a quasi-steady state with much longer relaxation times involved. In reality, of course, this would require tremendously long periods of time (tens of years to reach full equilibrium), so that any, even low volatile liquids, would be removed by evaporation or by chemical reactions. We note that while $s_f \approx s_0$, those two values are supposed to be always slightly different such that $s_f > s_0$. Parameter s_f corresponds to a steady state when the porous network is still connected through the liquid bridges, while at s_0 the connectivity of the porous network is supposed to be completely broken. To put this differently, s_0 in our model is assumed to be only related with the liquid distributed on the grain surface, while s_f also takes into account the bridges connecting the grains, see further discussion below.

At $\bar{s} \approx 10\%$ the increase of the wet volume with time becomes a power law $V(t) \propto t^{\lambda_3}$ with $\lambda_3 \approx 0.75$, that is the wetting front radius in this three-dimensional case behaves as $X_3(t) \propto t^{0.25}$. This power law has been previously identified to be universal for the pendular regime in the case of three dimensional geometry of wetting volumes [7].

One may notice that using reduced time t/t_0 with the scaling dictated by a diffusion law, that is $t_0 = \frac{V_D^{2/3}}{D_e}$, one can bring the evolution curves corresponding to different drop volumes V_D into a master curve. Parameter $D_e = 1.85 \times 10^{-10}\,\mathrm{m}^2/\mathrm{s}$ (effective coefficient of diffusion) has been chosen to get the reduced time at the beginning of the pendular regime of wetting; that is, the average saturation level $\bar{s} = 0.1$ occurs at $t/t_0 = 1$. The result indicates that macroscopically the process of spreading can be described by a diffusion-like model, which will be explored in the next parts.

In another set of experiments, we studied liquid spreading in essentially one-dimensional geometry, Fig. 6. As in the three dimensional geometry, the behaviour is characterized by an initial phase of liquid spreading and a power law corresponding to the main phase of the pendular regime, Fig. 7. As expected, the spreading is faster for the less viscous, well-wetting TBP liquid and slower for more viscous TCP liquid with a larger contact angle. We did not follow the moving front evolution to the standstill due to much longer characteristic times involved in one-dimensional cases, which are on the time scale of persistence of TBP [17].

The power law observed in the evolution of the moving front in the one-dimensional geometry, $X_1(t) \propto t^{0.5}$, and in the three-dimensional case, $X_3(t) \propto t^{0.25}$, suggests that in general there should be universal behaviour $X_n(t) \propto t^{1/(n+1)}$, where n designates the dimension of the experimental setup. In what follows, we examine these data on theoretical grounds.

III. MACROSCOPIC MODEL

Consider the pendular regime of wetting, when the liquid bridges are completely isolated and only connected via liquid films on the particle surfaces. In a macroscopic volume element containing many particles V, the averaged value of pressure in the pendular rings should be the same as the average pressure in the macroscopic liquid films in the creeping flow conditions. In each individual pendular ring, the pressure is a function of the liquid content. For example, for a liquid bridge formed between two identical spheres of radius R, one can find a closed form analytical solution relating surface shape,

Set	Liquid	μ (mPa · s)	γ (mN/m)	P_{ve} (Pa)	V_D (mm^3)	R (mm)	w_R (mm)	s_f (%)	$s_f - s_0^e$ (%)	$\delta_R(\mu$m)	D_f (10^{-14} m^2/s)	D_0^e (10^{-14} m^2/s)
I	TCP	20	42.5	8×10^{-5}	3	0.26	0.06	0.61	0.043	1	7 ± 1.6	7 ± 3.2
II	TCP	20	42.5	8×10^{-5}	6	0.26	0.06	0.61	0.043	1	7 ± 1.6	7 ± 3.2
III	TCP	20	42.5	8×10^{-5}	12	0.26	0.06	0.61	0.043	1	7 ± 1.6	7 ± 3.2
IV	TCP	20	42.5	8×10^{-5}	6	0.32	0.08	0.49	0.028	1	5.2 ± 1	4.7 ± 2.4
V	TCP	20	42.5	8×10^{-5}	6	0.2	0.06	0.73	0.073	1	6.4 ± 1	12 ± 7.2
VI	TCP	20	42.5	8×10^{-5}	6	0.14	0.04	1.16	0.15	1	4.9 ± 1	25 ± 14
VII	TBP	3.9	28	1.5×10^{-1}	6	0.25	0.08	0.68	0.046	1	100 ± 22	100 ± 64
VIII	TEHP	15	29	1.1×10^{-5}	6	0.25	0.08	0.68	0.046	1	33 ± 6	27 ± 17

TABLE I. Parameters of the drop spreading experiments: liquid viscosity μ at $20^\circ C$, surface tension γ at $25^\circ C$, equilibrium vapour pressure P_{ev} at $20^\circ C$ [17, 18], drop volume V_D, average grain radius R, standard deviation around the average grain radius w_R, steady state saturation level s_f, the model parameter $s_f - s_0^e$ calculated at $B_f = 29\,\mu$m^2 on the basis (25), the length scale of capillary pressure δ_R calculated using (17) and (25) at $B_f = 29\,\mu$m^2, coefficient of diffusion D_f obtained in the comparison with experimental data, coefficient of diffusion D_0^e calculated on the basis of (8), (29) and parameters of the liquids and the sands at $\delta_R = 1\,\mu$m, $\theta_c = 30^\circ$ in the case of TCP and $\theta_c = 0^\circ$ in the case of TBP and TEHP, and $\epsilon_p = 0.15$.

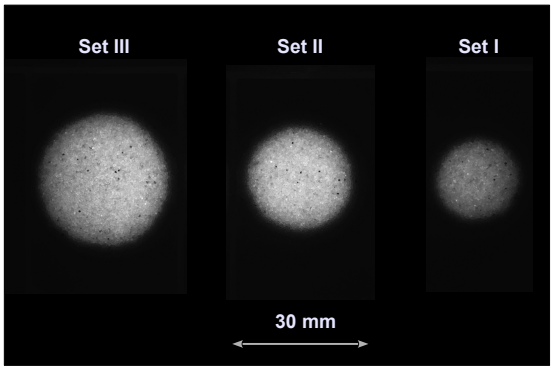

FIG. 4. UV fluorescence images of wet areas taken after $\approx$ 45000 min of spreading from above the sand bed prepared using $R \approx 0.26$ mm sand. From left to right the image is for the sets III, II and I, as in Table I.

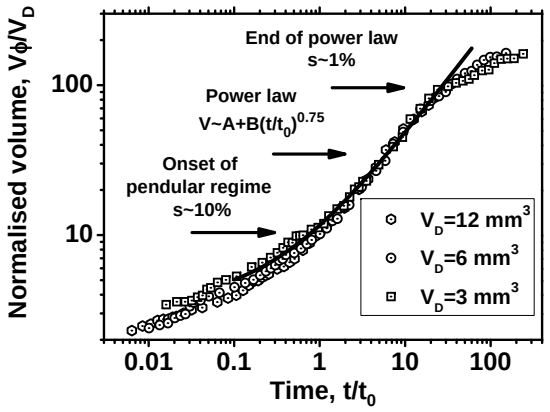

FIG. 5. Spreading of TCP liquid drops of different volumes $V_D = 3, 6$ and $12\,\text{mm}^3$ in $R \approx 0.26$ mm sand in a three-dimensional case. Normalized volume $V\phi/V_D$ (inverse average saturation $\bar{s}^{-1}$) as a function of reduced time t/t_0, where $t_0 = \frac{V_D^{2/3}}{D_e}$, $D_e = 1.85 \times 10^{-10}\,\text{m}^2/\text{s}$ ($t_0 \approx 300$ min at $V_D = 6\,\text{mm}^3$). The solid line is the fit $V\phi/V_D = A + B(t/t_0)^{0.75}$ at $A = 3.6$ and $B = 8$.

and hence the liquid volume contained in the ring, and the capillary pressure [5]. Even in this ideal case, the analytical expressions are quite lengthy, but, as we have verified numerically using results from [5], can be approximated at small contact angles $\theta_c \ll 1$ (between 0° and approximately 30°) via

$$p \approx p_0 \left\{ C_0 - C_1 \left(\frac{R^3}{V_B} \right)^{1/2} \right\} \qquad (2)$$

where $p_0 = \frac{2\gamma}{R}$, $C_0 = 3.7$ and $C_1 = 1.3$ [7]. One can see that with the liquid content increases, the capillary pressure tends to a constant value independent of saturation. This trend was observed in both spherical grains and real sieved sands [2]. Since in the pendular regime of wetting $s \ll 1$, the main pressure law in the model (2) can be further simplified to

$$p \approx -p_0\, C_1 \left(\frac{R^3}{V_B} \right)^{1/2}. \qquad (3)$$

To parametrize saturation, we split average liquid content in a sample volume V containing N grains into two parts: the liquid contained on the rough surface of particles of volume $V_r = 4\pi\alpha_R R^2 \delta_R N$ and the liquid contained in the capillary bridges $V_c = V_B N_c N$. Here, parameter N_c is the coordination number, that is the number of bridges per a particle. In our experiments the value of N_c was found to be around $N_c \approx 7$.

Combining both contributions, saturation $s = \dfrac{V_c + V_r}{\phi V}$ can be presented as

$$s = V_B R^{-3} A_s + s_0, \qquad (4)$$

where

$$A_s = \frac{3}{4} \frac{1-\phi}{\phi} \frac{N_c}{\pi}, \quad s_0 = 3\alpha_R \frac{1-\phi}{\phi} \frac{\delta_R}{R}.$$

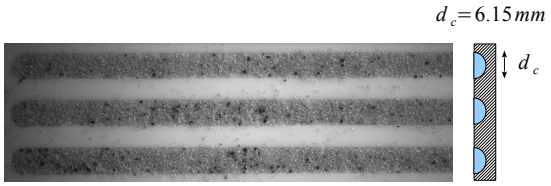

FIG. 6. Channels in Teflon (diameter of the hemicylinder $d_c = 6.15\,\mathrm{mm}$) filled in by the standard Ottawa sand ($R \approx 0.25\,\mathrm{mm}$) before depositing $V_D = 3\,\mathrm{mm}^3$ liquid drops.

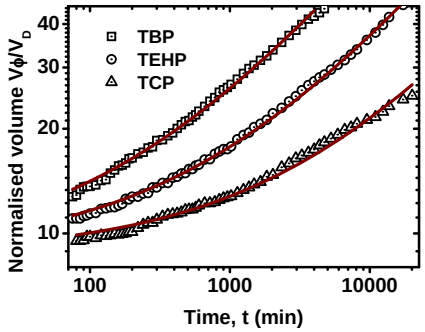

FIG. 7. Spreading of TCP, TEHP and TBP liquid drops ($V_D = 3\,\mathrm{mm}^3$) in $R \approx 0.25\,\mathrm{mm}$ sand in the channels, as in Fig. 6. Normalised wet volume $V\phi/V_D$ (inverse average saturation $\bar{s}^{-1}$) as a function of time. The experimental data are shown by symbols and the solid lines (brown) are the fits $V\phi/V_D = A + Bt^{0.5}$.

Using (3) and (4), the average capillary bridge pressure $P =< p >^l$ can be presented as

$$P = -p_0 \frac{C_1\, A_s^{1/2}}{(s - s_0)^{1/2}}, \tag{5}$$

where $< ... >^l = V_l^{-1} \int_{V_l} d^3x$ is intrinsic liquid averaging, V_l is liquid volume within the sample volume V. We have assumed previously in developing our preliminary theoretical model that parameter s_0 is constant, that is independent of the capillary pressure. This is a good approximation in a range of capillary pressures, but could be possibly violated at small values of $s \approx s_f \approx s_0$. Indeed, consider a model groove geometry shown in Fig. 8. Surface flows in that kind of geometry have been studied experimentally and theoretically in [10–12]. The liquid in this case is contained both inside the large scale grooves (large scale surface roughness), in capillary menisci, and on the surface with much smaller scale roughness. At very large capillary pressure, the meniscus curvature could be much

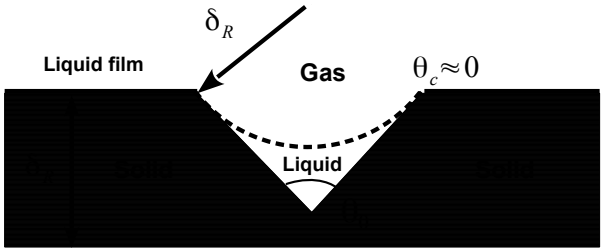

FIG. 8. Illustration of the model groove geometry with an opening angle θ_0 and a contact angle θ_c used in the estimations of κ_0 and s_0. In the illustration, the capillary pressure is $p = -\gamma/\delta_R$, the opening angle $\theta_0 = \pi/2$ and the contact angle $\theta_c = 0^\circ$ (complete wetting).

lower then the characteristic length scale of the groove, so that the groove would be only partially filled in. On the other hand, at very low capillary pressure, the radius of curvature could be much larger than the size of the groove, and the groove would be fully saturated with the liquid. Consider some numerical example. At $s = s_c = 10\%$ taking $R = 250\,\mu\mathrm{m}$ and $s_0 = 0.6\%$ from (5) the radius of curvature of the meniscus in Fig. 8 would be around $16\,\mu\mathrm{m}$. This value is much larger than the surface roughness amplitude (the maximum size of the grooves) in our sand grains, about $\max(\delta_R) \approx 3\,\mu\mathrm{m}$, so that the groove can be assumed to be fully filled in. But as s tends to s_f, the radius of curvature would be comparable to the characteristic length scale of the groove, as is shown in Fig. 8. If we assume a linear relationship $s_0 = B_0(s - s_f) + s_0^e$, where $B_0 = \frac{s_0^m - s_0^e}{s_c - s_f}$, such that s_0 changes in between some minimum value s_0^e corresponding to partially saturated grooves and some maximum value s_0^m corresponding to fully saturated grooves, $s_0^e \le s_0 \le s_0^m$, while s is changing from s_f to s_c, then

$$\frac{P}{p_0} = -\frac{C_1\, A_s^{1/2}}{(1 - B_0)^{1/2}(s - s_0^e)^{1/2}} = -\frac{P_c}{(s - s_0^e)^{1/2}}. \tag{6}$$

The minimum value of s_0, as it has been found in our experiments, is about $s_0^e = 3\alpha_R \frac{1-\phi}{\phi}\frac{\delta_R}{R} \approx 0.6\%$, while the maximum value s_0^m should be bounded $s_0^m < \frac{3}{2}\frac{1-\phi}{\phi}\frac{\max(\delta_R)}{R} \approx 4\%$. Since $s_c \gg s_0^m$, this introduces a small correction to the coefficient in the pressure law, $B_0 \ll 1$, and parameter s_0^e is now taken at the equilibrium value.

Consider now the local transport on the surface of particles. The surface flux density $\mathbf{q}$, according to the previous study of liquid spreading on rough surfaces made of microscopic grooves of various shapes and di-

mensions [19, 20], obeys a Darcy-like law

$$\mathbf{q} = -\frac{\kappa_m}{\mu}\nabla\psi, \tag{7}$$

where μ is liquid viscosity, ψ is local pressure in the liquid averaged within the surface roughness and $\kappa_m = \kappa_0\delta_R^2$ is the effective coefficient of permeability of the surface roughness, which is proportional to the square of the length scale parameter δ_R. To understand the order of magnitude of $\kappa_m = \kappa_0\delta_R^2$, one can again consider the surface groove of a simplified geometry, as is shown in Fig. 8. We note, that the fluid flow mostly occurs within large scale surface grooves. Then, assuming a fully developed rectilinear Hagen-Poiseuille flow in the open channel at $\theta_0 = \pi/2$ and $\theta_c = 0$, Fig. 8, and the results of analysis of liquid flows in corners in [21], $\kappa_0 = \frac{\varepsilon_0}{\beta_1}\left(1 - \frac{\pi}{4}\right)$, where non-dimensional parameter β_1 was found to be $\beta_1 \approx 100$ [21] and parameter $\varepsilon_0 < 1$ is the ratio of the total cross sectional area of the grooves to the total cross sectional area of the surface layer of width δ_R. Due to the capillary pressure variations in the grooves and, as a consequence, variations of the cross-section area of the groove volume occupied by the liquid, parameter κ_0 would vary in the idealized case between $\frac{\varepsilon_0}{\beta_1}\left(1 - \frac{\pi}{4}\right) \le \kappa_0 \le \frac{\varepsilon_0}{\beta_2}$, where parameter β_2 in the case of a fully saturated groove was found to be $\beta_2 \approx 50$ [21]. This implies that $\kappa_0 = \kappa_0(s)$. When s changes from s_f to s_c, assuming again a linear relationship

$$\kappa_0(s) = \frac{\kappa_0^2 - \kappa_0^1}{s_c - s_f}(s - s_f) + \kappa_0^1,$$

$$\kappa_0^1 = \frac{\varepsilon_0}{\beta_1}\left(1 - \frac{\pi}{4}\right), \quad \kappa_0^2 = \frac{\varepsilon_0}{\beta_2}.$$

The minimum value of the channel permeability is defined by the maximum capillary pressure in the system. We note, while in unbounded V-shaped grooves, especially at small opening angles θ_0, the free surface is also unbounded, so that the capillary spreading in the absence of external forces, like the gravity force, is unbounded, in our case, a quasi-steady state is observed corresponding to the maximum capillary pressure [22]. If the contact angle θ_c is not equal to zero, then the amount of the liquid contained in the groove at a fixed value of pressure, that is at a fixed value of δ_R is reduced. Then

$$\kappa_0^1 = \frac{\varepsilon_0}{\beta_1}\left(\cos\theta_c(\cos\theta_c - \sin\theta_c) - \frac{\pi}{4} + \theta_c\right), \quad \kappa_0^2 = \frac{\varepsilon_0}{\beta_2}.$$

One needs to note that those estimates ignore any contributions from tortuosity and other details of the open channel geometries, which may substantially reduce (or change) the value of the channel permeability [11, 21, 23]. For example, a change in the groove corner opening angle θ_0, as is shown in Fig. 8, may result in almost an order of magnitude change of the surface permeability of the channel [11, 21]. So that we introduce an adjusting parameter ϵ_p of the model, which will be determined on the basis of comparison with experimental observations, so that

$$\kappa_0^1 = \frac{\varepsilon_p}{\beta_1}\left(\cos\theta_c(\cos\theta_c - \sin\theta_c) - \frac{\pi}{4} + \theta_c\right), \tag{8}$$

$$\kappa_0^2 = \frac{\varepsilon_p}{\beta_2}.$$

Parameter $\varepsilon_p < 1$ incorporates parameter $\varepsilon_0 < 1$ and effects of tortuosity and the opening groove angle θ_0. The parameter also takes into account that some grooves while filled in with the spreading liquid may be dead ends, so that they do not participate with liquid conductivity. Realistically, considering that at least $\varepsilon_0 < 0.5$ (that is only half of the surface area is likely to be available for the liquid) and that the tortuosity can reduce permeability at least two-fold, $\varepsilon_p < 0.25$. Further improvement of the model may require careful implementation of the surface groove, surface roughness flow details [11, 21].

According to the spatial averaging theorem [24], applying intrinsic liquid averaging $< ... >^l$

$$-\frac{\kappa_m}{\mu}\left\{\nabla < \psi >^l + V_l^{-1}\int_{S_l}\psi\,\mathbf{n}\,dS\right\} =< \mathbf{q} >^l, \tag{9}$$

where S_l is the area of the liquid interface confined inside the volume element V and with normal vector $\mathbf{n}$. The surface integral in the creeping flow conditions, when the pressure variations across the liquid layer are insignificant, can be neglected $V_l^{-1}\int_{S_l}\psi\,\mathbf{n}\,dS \approx 0$ and

$$-\frac{\kappa_m}{\mu}\nabla < \psi >^l =< \mathbf{q} >^l . \tag{10}$$

Now, one can cast the continuity equation, presuming conservation of mass, that is neglecting evaporation processes,

$$\frac{\partial\phi s}{\partial t} + \nabla\mathbf{Q} = 0$$

into

$$\frac{\partial\phi s}{\partial t} = \nabla\left\{\frac{K}{\mu}\nabla P\right\}. \tag{11}$$

Here,

$$\mathbf{Q} = \frac{S_e}{S} < \mathbf{q} >^l, \tag{12}$$

S is the surface area of the sample volume V with the effective area of entrances and exits S_e and coefficient $K = \kappa_m\frac{S_e}{S}$. It is assumed that in the creeping flow conditions $P =< p >^l \approx < \psi >^l$. Note, that the ratio S_e/S is not strictly speaking just a geometric factor. It is an average quantity defined by (12), which incorporates connectivity and the shape of the surface elements.

We note, that the effects of gravity have been neglected in the model. To understand the accuracy of

this approximation, we first notice that, the capillary pressure, in our case, is assumed to be generated on a length scale $\delta_R \sim 1\,\mu$m, which is comparable with the length scale of the surface roughness. If we now compare the capillary length $l_c = \sqrt{\gamma/\rho g} \sim 2\,$mm, where ρ is liquid density and g is the gravity constant, with the length scale associated with the gradient of capillary pressure $\sqrt{\delta_R L_0}$, where $L_0 \sim 10\,$mm is the characteristic length scale of the wetting area in our experiments, then $l_c \gg \sqrt{\delta_R L_0} \sim 0.1\,$mm. This implies that the gravity effects can be ignored. At the same time, the length scale associated with the gradient of capillary pressure $\sqrt{RL_0}$ in the funicular regime may be comparable with l_c so that the accuracy of our approximation may be reduced.

Assuming further that porosity ϕ is constant and using expression (6) for the average pressure, one can transform the governing equation (11) into a non-linear diffusion equation for the saturation $s(\mathbf{x}, t)$

$$\frac{\partial s}{\partial t} = \nabla \left\{ \frac{D_s \nabla s}{(s - s_0^e)^{3/2}} \right\}, \tag{13}$$

where

$$D_s = \frac{1}{2} \frac{K}{\mu} \frac{p_0 P_c}{\phi}.$$

To address a moving boundary value problem set in an open domain with a smooth boundary $\partial\Omega$ moving with velocity $\mathbf{v}$, the governing equation (13) is complemented with the boundary conditions

$$s|_{\partial\Omega} = s_f, \quad s_f > s_0^e \tag{14}$$

and

$$\mathbf{v} \cdot \mathbf{n}|_{\partial\Omega} = v_n|_{\partial\Omega} = -D_s \frac{\mathbf{n} \cdot \nabla s}{s_f (s_f - s_0^e)^{3/2}}, \tag{15}$$

where $\mathbf{n}$ is the normal vector to the boundary $\partial\Omega$. The boundary value of the saturation s_f is defined by the capillary pressure developed at the moving front. To be precise, the inverse of the reduced capillary pressure (capillary pressure normalized by $2\gamma/R$) is related with the difference of two parameters $s_f - s_0^e$. Parameter s_f defines a steady state saturation level, when the network connectivity is reduced but not broken, while parameter s_0^e can be associated with the saturation levels, when the network connectivity is broken.

To get an estimate of the typical values of the boundary pressure and the saturation, we assume that the pressure is generated by the capillaries with a characteristic size of the order of δ_R. Then, for example for TCP liquid, taking characteristic value of the surface tension $\gamma = 42.5\,$mN/m at 25° C, one can obtain that at $\delta_R = 1\,\mu$m the capillary pressure $|P| = \dfrac{\gamma}{\delta_R} = 4.25 \times 10^4\,$Pa. As a result, from (6), taking typical parameter values $R = 250\,\mu$m and $\phi = 0.3$, parameter $s_f - s_0^e \approx 4 \times 10^{-4}$, which is close to the values found in the previous analysis of experimental data in [7]. Note that $\frac{s_f - s_0^e}{s_0^e} \ll 1$, considering that $s_0^e \approx 0.006$.

In general, using (6), one can obtain the following scaling

$$s_f - s_0^e = 4P_c^2 \left(\frac{\delta_R}{R} \right)^2. \tag{16}$$

That is, taking into account (1)

$$s_f = 3\alpha_R \frac{1-\phi}{\phi} \frac{\delta_R}{R} + 4P_c^2 \left(\frac{\delta_R}{R} \right)^2. \tag{17}$$

A. Global surface permeability of a system of spherical particles.

To simulate liquid spreading with the help of (13), the coefficient of permeability K and hence the parameter S_e/S need to be determined.

To obtain an estimate of these parameters, we consider just one single particle with a closed surface Γ, which is split into three sub-domains Ω_0, Ω_1 and Ω_2 with the surface boundaries between them $\partial\Omega_1$ and $\partial\Omega_2$, Fig. 9. The sub-domains Ω_1 and Ω_2 correspond to the area covered by the liquid in the bridges, while the surface flow, described by (7), takes place in Ω_0.

The transport process in the surface layer of the granular elements is described by a Darcy's like law (7). The liquid is assumed to be incompressible, that is $\nabla \cdot \mathbf{q} = \mathbf{0}$, and the capillary pressure variations on the scale of one grain particle are assumed to be small enough, so that $\kappa_m \approx const$. The problem then can be reduced to a boundary-value problem for the Laplace-Beltrami equation

$$\Delta_{\Omega_0} \psi = 0 \tag{18}$$

defined on the surface element Ω_0 of the particle.

At the same time, liquid pressure variation in the bridges is negligible in slow creeping flows in comparison to that in Ω_0. So that, one can assume that

$$\psi|_{\partial\Omega_1} = \psi_1 = const, \quad \psi|_{\partial\Omega_2} = \psi_2 = const, \tag{19}$$

The boundary-value problem (18)-(19) has a unique solution, which, if it is found, allows to calculate the total flux Q_T through any contour $\partial\Omega$ on Ω_0, which can not be contracted to a point

$$Q_T = \delta_R \frac{\kappa_m}{\mu} \int_{\partial\Omega} \mathbf{n} \cdot \nabla\psi \, dl,$$

where $\mathbf{n}$ is the normal vector to the contour $\partial\Omega$ on the surface, δ_R is the average amplitude of the surface roughness, that is the width of the surface layer conducting the liquid flux, and we assumed that ψ is roughly constant across the liquid layer. In particular, due to the conservation of the liquid and in a steady state

$$Q_T = \delta_R \frac{\kappa_m}{\mu} \int_{\partial\Omega_1} \mathbf{n} \cdot \nabla\psi \, dl = -\delta_R \frac{\kappa_m}{\mu} \int_{\partial\Omega_2} \mathbf{n} \cdot \nabla\psi \, dl.$$

To obtain analytical results, we restrict ourselves to the case of a spherical particle of radius R. In this case, domain boundaries $\partial\Omega_1$ and $\partial\Omega_2$ will be circular cross sections of the spherical surface Γ, Fig. 9. The location of the sub-domains Ω_1 and Ω_2 with respect to each other on the surface is fixed by an angle β. We consider an azimuthally symmetric case, $\beta = \pi$, with equal in size (radius of curvature) domain boundaries $\partial\Omega_1$ and $\partial\Omega_2$, as is shown in Fig. 9. Then, due to the nature of the boundary conditions (19), the problem (18)-(19) is equivalent to

$$\frac{1}{\sin\theta}\frac{\partial}{\partial\theta}\left(\sin\theta\frac{\partial\psi}{\partial\theta}\right) = 0, \quad \theta_0 \le \theta \le \pi - \theta_0, \tag{20}$$

with the boundary conditions

$$\psi|_{\theta=\theta_0} = \psi_1, \quad \psi|_{\theta=\pi-\theta_0} = \psi_2, \tag{21}$$

where we used a spherical coordinate system with the polar angle θ counted from the axis of symmetry.

The problem (20)-(21) admits an analytical solution, which is, after applying the boundary conditions,

$$\psi = \frac{\psi_2 - \psi_1}{2}\left\{1 - \frac{\ln\frac{\sin\theta}{1+\cos\theta}}{\ln\frac{\sin\theta_0}{1+\cos\theta_0}}\right\} + \psi_1.$$

One can now calculate the total flux

$$Q_T = -2\pi\delta_R\,\frac{\kappa_m}{\mu}\sin\theta_0\,\frac{\partial\psi}{\partial\theta}\bigg|_{\theta=\theta_0}$$

$$= -\pi\delta_R\,\frac{\kappa_m}{\mu}\frac{\psi_2 - \psi_1}{\ln\frac{1+\cos\theta_0}{\sin\theta_0}}.$$

One can define the effective coefficient of permeability of a sphere K_1, which is approximately equivalent to K, by

$$Q_T = -4R\,(\psi_2 - \psi_1)\frac{K_1}{\mu}$$

so that

$$K_1 = \frac{\delta_R}{4R}\frac{\pi\kappa_m}{\ln\frac{1+\cos\theta_0}{\sin\theta_0}}.$$

One can see that the permeability coefficient K_1 is divergent at $\theta_0 = \pi/2$ and tends to zero at $\theta_0 = 0$ as expected, that is

$$K_1 \to \frac{\delta_R}{4R}\frac{\pi\kappa_m}{\frac{\pi}{2} - \theta_0} \quad \theta_0 \to \frac{\pi}{2}$$

and

$$K_1 \to -\frac{\delta_R}{4R}\frac{\pi\kappa_m}{\ln\theta_0} \quad \theta_0 \to 0.$$

In what follows, we approximate the coefficient of permeability K by K_1 obtained in an azimuthally symmetric case. To incorporate K_1 into the model, we should express it through the saturation s. Using an approximate relationship between the radius of curvature $R\sin\theta_0$ of the boundary contour $\partial\Omega_1$ and the pendular ring volume [1], one can get

$$\sin^2\theta_0 \approx \sqrt{s - s_0^e}.$$

That is at $\theta_0 \ll 1$ or $(s - s_0^e) \ll 1$,

$$K_1 \approx \frac{\delta_R}{R}\frac{\pi\kappa_m}{|\ln(s - s_0^e)|}.$$

So, finally, (13) becomes

$$\frac{\partial s}{\partial t} = \nabla\left\{\frac{D_0\,\nabla s}{|\ln(s - s_0^e)|(s - s_0^e)^{3/2}}\right\}, \tag{22}$$

where

$$D_0 = \frac{\delta_R^3}{R^2}\frac{\pi\kappa_0(s)}{\mu}\frac{\gamma\,P_c}{\phi}.$$

B. Self-similarity and superfast diffusion

The obtained non-linear partial differential equation is known in mathematical literature as the superfast nonlinear diffusion equation, which has distinctive mathematical properties [25]. In particular, it is well known that many non-linear diffusion models, such as the porous medium equation, exhibit the so called self-similar behaviour, which allows to obtain universal long-time limiting asymptotic solutions. For example, there are compactly supported Barenblatt self-similar distribution profiles satisfying a natural set of boundary conditions with finite velocity of the moving boundary [26–29]. These asymptotic distributions are very useful in practical applications, since solutions to the porous medium equations of different types are practically independent of initial conditions and ultimately tend to the asymptotic distributions with time [27–29].

But, this is not the case here. The super-fast diffusion model in our case does not demonstrate this universal behaviour. While initial distributions of saturation evolve with time to a distinctive saturation profile (as we will discuss later in detail), there was no true self-similar behaviour identified in our simulations so far. Indeed, consider a simplified non-dimensional version of (22) in a one-dimensional domain $\Omega \subset \mathbb{R}$ with the boundary $\partial\Omega$ moving with velocity v. Neglecting relatively slow variations of κ_0 with saturation, one has

$$\frac{\partial u}{\partial t} = \frac{\partial}{\partial x}\left\{\frac{(u + u_0)^{-\frac{3}{2}}}{\ln(u + u_0)}\,\frac{\partial u}{\partial x}\right\}, \quad x \in \Omega,\ \ t > 0$$

with

$$u|_{\partial\Omega} = 0 \tag{23}$$

and

$$v|_{\partial\Omega} = -\frac{1}{s_f}\frac{u_0^{-\frac{3}{2}}}{\ln u_0}\frac{\partial u}{\partial x}\bigg|_{\partial\Omega}, \qquad (24)$$

where $u = s - s_f$ and $u_0 = s_f - s_0^e$. Consider a one-parameter group of transformations of the variables $t \to \epsilon t$, $u \to \epsilon^q u$ and $x \to \epsilon^m x$, which is used to obtain self-similar solutions, in particular the Barenblatt self-similar distribution profiles; $\epsilon > 0$. One can immediately see that the moving boundary value problem is not invariant under the group of transformations, that is one can not determine such q and m at $u_0 \neq 0$ so that to obtain an invariant equation with invariant boundary conditions. This conclusion is consistent with our numerical simulations, where no global self-similar behaviour of the distribution profiles $s(\mathbf{x}, t)$ with time has been identified so far.

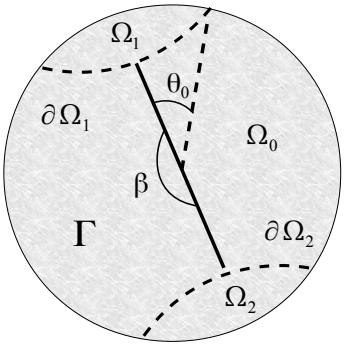

FIG. 9. Illustration of the surface diffusion domains.

IV. RESULTS AND DISCUSSION

In this part, we consider and discuss applications and comparisons of the developed macroscopic model with our experimental data. First, we analyse steady states of the spreading process, that is the final extends of the spreading volumes, in three-dimensional spherically symmetric geometry. We will discuss and demonstrate how steady state data can be used to obtain estimates of the model parameters s_f and $s_f - s_0^e$. We will also evaluate the effects of evaporation. Next, we augment our superfast diffusion model to extend its applicability domain to the entire funicular regime of spreading. We will discuss saturation profiles and their intimate connection with the universal power law of liquid spreading observed in the experiments. To verify the fidelity of our approach and the mathematical model, we consider spreading and compare with the experiments in one-dimensional geometry using parameter set obtained in the three-dimensional experiments and comparisons. Finally, we will analyse liquid spreading in pre-wet porous matrices.

A. Steady state distributions

Consider final extends of spreading obtained in a series of experiments with TCP liquid drops placed on sands with different grain sizes R, that is sets II, IV, V, and VI, details in Table I. The dependence of the equilibrium saturation in the end of the spreading process, s_f, on the inverse particle radius R^{-1} is shown in Fig. 10. Assuming scaling (17), we fit the dependence by a function

$$s_f = s_0^e + B_f R^{-2} = A_f R^{-1} + B_f R^{-2} \qquad (25)$$

with $A_f = 1.5\,\mu\text{m} \pm 0.2\,\mu\text{m}$ and $B_f = 29\,\mu\text{m}^2 \pm 24\,\mu\text{m}^2$. This implies that one can only determine one parameter with sufficient accuracy, and place upper and lower bounds for the other parameter.

Then, using obtained value of A_f and the most probable value of B_f, from (17), one can determine δ_R and α_R. From $A_f = 3\alpha_R \frac{1-\phi}{\phi}\delta_R$ using $\phi = 0.3$, one gets $\alpha_R\delta_R \approx 0.2\,\mu$m. Then, from $B_f = 4P_c^2\delta_R^2$, one can estimate that $\delta_R \approx 1\,\mu$m and $\alpha_R \approx 0.2$.

The equilibrium value of saturation s_f observed in the spreading of TEHP drops is consistent with the above estimates, while the observed value for TBP is slightly off. Indeed, the equilibrium level of TEHP in $R = 0.25\,$mm sand was found to be $s_f \approx 0.68\%$, while the value of $s_f = 0.67\%$ was expected according to (17). At the same time, the final saturation level of TBP in the sand with the same average grain radius, estimated assuming conservation of mass of the liquid, was found to be at much higher level $s_f = 0.93\%$ after about 6 days of spreading. Such deviation is likely to be due to much higher equilibrium vapour pressure of TBP, Table I, and hence much higher evaporation rates involved in this case. The larger value of s_f suggests that about 27% of the liquid had been removed by evaporation. This is qualitatively consistent with our experimental estimate of TBP persistence in the one-dimensional case (with two times larger surface to volume ratio) equal to approximately 10 days (almost total evaporation). This in turn is quantitatively consistent with an estimate of evaporation rates calculated on the basis of the vapour pressure in quiescent conditions [30]. Indeed, the evaporation rate at $P_{ve} = 0.15\,$Pa in quiescent conditions (no air flow) for TBP (molar weight $266.32\,$g/mol) is $\approx 5.84 \times 10^{-2}\,$g/m^{2}h [30]. Then, given the characteristic surface area of the wet spot of about $3 \times 10^{-4}\,$m^2, the amount of liquid equivalent to a quarter of a liquid drop $V_D = 6\,$mm^3 would evaporate in about three days. Note, this is an upper estimate given that the spot radius is growing during the spreading, so that in reality this liquid amount would be removed by evaporation in about six days.

B. The dynamics of spreading

To understand the dynamics of liquid spreading and evolution of the moving front, that is the wetting volume, consider the superfast diffusion model (22). One

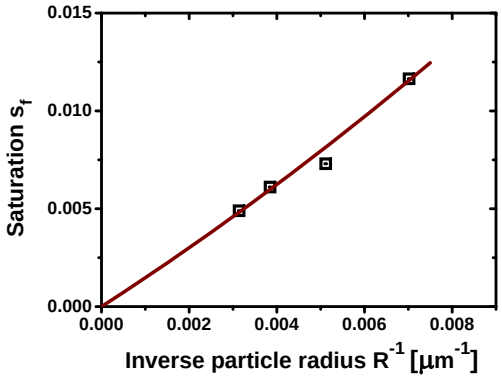

FIG. 10. Saturation s_f as a function of R^{-1} shown by symbols. The solid line is the fit $s_f = A_f R^{-1} + B_f R^{-2}$ at $A_f = 1.5\,\mu$m and $B_f = 29\,\mu$m^2.

can present (22) in non-dimensional form by normalizing distances $\tilde{\mathbf{x}} = \mathbf{x}/L_0$ and time $\tilde{t} = t/t_0$. As the characteristic length scale, we use the wet spot radius L_0 at some moment of time, which will be initial time for simulations $\tilde{t} = 0$, and $t_0 = L_0^2/D_0^e$. Then, omitting tilde in the notations, equation (22) can be presented as

$$\frac{\partial s}{\partial t} = \nabla \left\{ \frac{\widehat{\kappa_0}(s)\,\nabla s}{|\ln(s - s_0^e)|(s - s_0^e)^{3/2}} \right\}, \tag{26}$$

with two boundary conditions

$$s|_{\partial\Omega} = s_f \tag{27}$$

and

$$v_n|_{\partial\Omega} = -\frac{\widehat{\kappa_0}(s)\ (\mathbf{n}\cdot\nabla)s}{s_f|\ln(s_f - s_0^e)|(s_f - s_0^e)^{3/2}}. \tag{28}$$

Here

$$D_0^e = \frac{\delta_R^3}{R^2}\frac{\pi\kappa_0^1}{\mu}\frac{\gamma\, P_c}{\phi} \tag{29}$$

and

$$\widehat{\kappa_0}(s) = \frac{\kappa_0^2/\kappa_0^1 - 1}{s_c - s_0^e}\,(s - s_0^e) + 1$$

in

$$s_0^e \le s \le s_c$$

otherwise

$$\widehat{\kappa_0}(s) = \kappa_0^2/\kappa_0^1.$$

So, the problem has three essential non-dimensional parameters $s_f, s_f - s_0^e$ and V_D/L_0^3. The last parameter only contributes through the initial profile of saturation $s(\mathbf{x}, 0)$ at $t = 0$. We have already seen that variations of initial drop volume V_D at $s_f = const$ and $s_f - s_0^e = const$ result in self-similar behaviour, such that evolution curves of the moving front collapse on a single master curve after re-normalizing time t by a factor of $V_D^{2/3}$. This implies that one can further assume that $L_0^3 \propto V_D$, so that parameter L_0 can be solely defined by the initial drop volume V_D. This leaves us with just two non-dimensional parameters.

The role of parameter s_f is clear, it defines the final level of saturation and the final size of the wetting zone in porous media after the spreading comes to standstill. To understand the role of the remaining parameter $s_f - s_0^e$, which represents the capillary action, that is the inverse of the reduced capillary pressure at the moving front, consider numerical solutions to the problem. The details of the numerical moving mesh method can be found in the appendix.

C. Augmented superfast diffusion model

In the experiments, only the spot wetting area is measured giving the average value of saturation, while accurate estimation of the liquid distribution is still unattainable. This implies that the initial saturation profile at the onset of the pendular regime of wetting is basically unknown and should be simulated starting from a liquid distribution at much higher saturation levels $s > 10\%$, that is in the funicular regime of wetting, where the permeability is also a function of saturation [31].

To obtain realistic distributions of the liquid at the onset of the pendular regime of wetting, we augment the diffusion law (26) using empirical permeability relationships found in sands [31]. In unsaturated porous media (in particular in sands) at high saturation values, permeability decreases very fast with liquid saturation $\log_{10} K \propto s$, as it could be anticipated, such that the augmented diffusion law takes the form

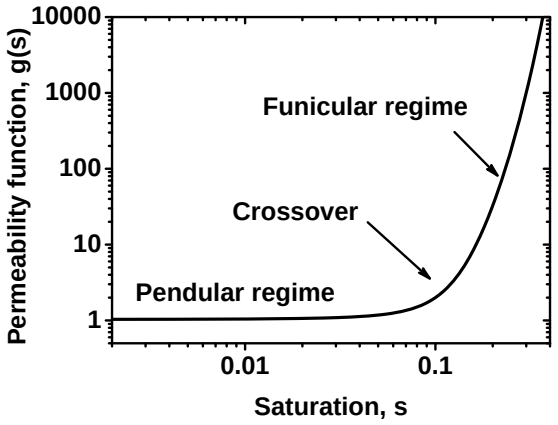

FIG. 11. Permeability function $g(s)$ versus saturation s at $\alpha_g = 16.5$, $\beta_g = 1.65$ and $f_0 = 1$.

$$\frac{\partial s}{\partial t} = \nabla \left\{ \frac{\widehat{\kappa_0}(s)\, g(s)\, \nabla s}{|\ln(s - s_0^e)|(s - s_0^e)^{3/2}} \right\}, \qquad (30)$$

where augmenting permeability function $g(s)$, Fig. 11,

$$g(s) = 1 + f_0\, 10^{\alpha_g s - \beta_g} \qquad (31)$$

with

$$\alpha_g = 16.5,\ \beta_g = 1.65$$

and

$$f_0 = \left(\frac{R}{R_m}\right)^2 \frac{\gamma}{\mu}\frac{\mu_w}{\gamma_w}. \qquad (32)$$

The values of the coefficients in (31) have been chosen such that, according to [31], in the medium fine sands ($R_m \approx 260\,\mu$m) and water (surface tension γ_w and viscosity μ_w)

$$g(s)\mid_{s=0.1} = 2, \quad g(s)\mid_{s=0.3} = 2000$$

and $f_0 = 1$. As one can see, Fig. 11, the augmenting function $g(s)$ due to the strong decline with the saturation has a very short crossover region quickly reaching a constant value $g(s) \approx 1$ at $s \approx 0.1$, where the pendular regime begins. We note that we still use pressure-saturation relationship (6), which provides a reasonable approximation considering strong variations of permeability. Alternatively, the model can be easily generalized by using a Leverett J-function [32].

D. Numerical simulations and experimental results in three-dimensional spherically symmetric cases

To compare numerical solutions of the superfast diffusion model (30) with experimental observations, we first consider simulations in a three-dimensional spherically symmetric case, where saturation $s(r,t)$ is a function of time and the radius r in a spherical coordinate system with its origin at the centre of the hemisphere representing the wet volume, Fig. 4. We have started our simulations in this case with

$$s(r,t)\mid_{t=0} = s_f + s_a \cos^{\lambda_a}(\pi r/2), \ \ 0 \le r \le 1 \qquad (33)$$

at different values of parameters $0.2 \le s_a \le 1 - s_f$ and $0.2 \le \lambda_a \le 0.4$. The value of L_0 then is defined by conservation of the liquid, neglecting the evaporation effects,

$$2\pi\phi \int_0^1 s(r,0)\, r^2\, dr = V_D L_0^{-3}.$$

We note, that due to the use of a spherical coordinate system, we also require that at $r = 0$ the first derivative $\partial s/\partial r = 0$ to avoid singular spurious solutions.

The choice of parameter s_a in the initial distribution and even its functional form is not obvious. We observed in the experiments that just in about ten minutes of spreading, the wetting spot volume shape becomes spherically symmetric, when the average saturation level $\bar{s} \approx 0.5$, Fig. 5. But what is the liquid distribution at this stage?

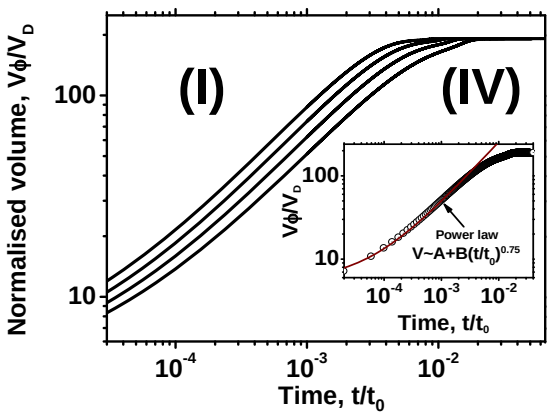

FIG. 12. Simulation of spreading in a three-dimensional spherically symmetric case using augmented superfast diffusion model (30) with initial distribution (33) at $\lambda_a = 0.3$, $s_a = 0.4$, $\alpha_g = 16.5$, $\beta_g = 1.65$, $f_0 = 1$ and $s_f = 0.0052$, but at different values of parameter $s_f - s_0^e$. Normalised wet volume $V\phi/V_D$ (inverse average saturation $\bar{s}^{-1}$, solid lines) as a function of the reduced time t/t_0, $t_0 = L_0^2/D_0^e$. From left to right: (I) $s_f - s_0^e = 0.0001$, (II) $s_f - s_0^e = 0.0002$, (III) $s_f - s_0^e = 0.0004$, (IV) $s_f - s_0^e = 0.0008$. Insert shows the power law $V\phi/V_D = A + B(t/t_0)^{0.75}$ (solid line, brown) in comparison with the numerical data (symbols, black) at $s_f - s_0^e = 0.0008$.

If we fix parameters of the initial distribution (s_a and λ_a) and parameter s_f, then evolution of the moving front at different values of $s_f - s_0^e$ represents a family of curves shown in Fig. 12. One may notice that, first of all, the smaller is the parameter $s_f - s_0^e$ (that is the higher is the reduced capillary pressure at the moving front) the faster the spreading occurs. Secondly, the power law found in the experiments $V \propto A + B(t/t_0)^{0.75}$ is very well observed in the simulations, see insert in Fig. 12.

As one can see from the distribution of the liquid at $t > 0$, Fig. 13 (a)-(b), the saturation profile quickly relaxes to a universal distribution at fixed values of s_f, $s_f - s_0^e$ and V_D. The distribution $s(r,t)$ at $t = t_2 = 6 \times 10^{-5}$, when the average value of saturation is already $\bar{s} \approx 0.1$, does not depend much on the details of the initial conditions. This implies that we may not need to worry about the initial profile in the simulations as far as the spreading at low saturation levels is concerned. The profile shape is very distinctive and is in good qualitative agreement with direct nuclear magnetic resonance imaging of inflow in porous materials such as gypsum building plaster, Portland lime stone and Portland cement [33]. It is flat in the central part, where the saturation levels are still in the funicular regime, and sharply declines to the boundary value $s = s_f$ through a zone with an accentuated

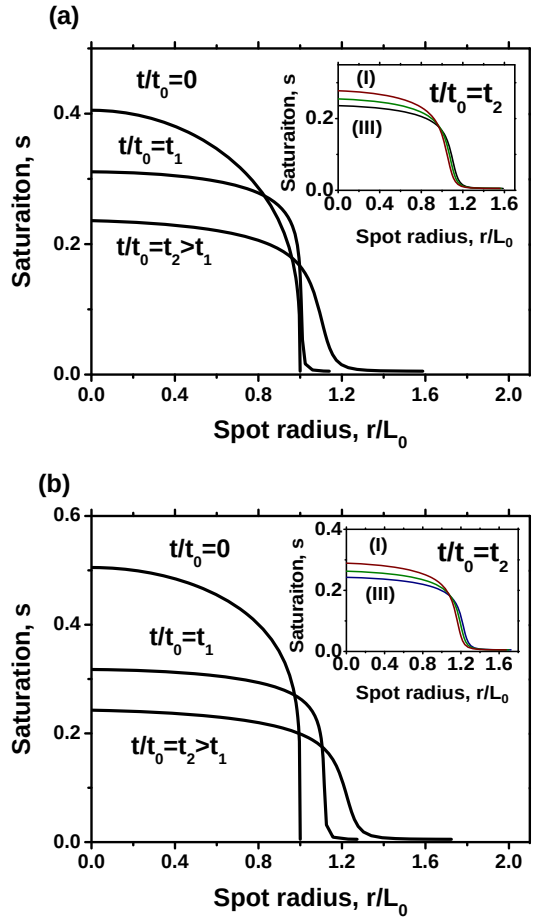

FIG. 13. Simulation of spreading in a three-dimensional spherically symmetric case using augmented superfast diffusion model (30) at different initial distributions (33). Saturation $s(r,t)$ as a function of the reduced spot radius r/L_0 at $t/t_0 = 0$, $t/t_0 = t_1 = 3\times10^{-6}$ and $t/t_0 = t_2 = 6\times10^{-5}$ at fixed values of $\alpha_g = 16.5$, $\beta_g = 1.65$, $f_0 = 1$, $s_f = 0.0052$ and $s_f - s_0^e = 0.0002$. (a) $\lambda_a = 0.3$ and $s_a = 0.4$; (b) $\lambda_a = 0.2$ and $s_a = 0.5$. The inserts show variation of the saturation profile at $t = t_2$ with the parameters of the augmenting function $g(s)$. Here (I) $\alpha_g = 12.5$ and $\beta_g = 1.25$, (II) $\alpha_g = 14.5$ and $\beta_g = 1.45$, and (III) $\alpha_g = 16.5$ and $\beta_g = 1.65$.

tail, where the saturation levels are characteristic to the pendular regime of wetting. We note that the saturation profile with the value in the central part $s \approx 0.3$ already corresponds to an average saturation level $\bar{s} \approx 0.1$. This implies that, first of all, there is no purely pendular or funicular regimes of spreading in dry porous materials and both mechanisms are in operation simultaneously. The overall dynamics of the wetting spot area seems to be defined to the large extent by the superfast diffusion processes in the tail region of the saturation distribution, while the role of the standard diffusion mechanisms inherent to the funicular regime is to level the liquid distribution by smoothing the profile in the central part. This can be directly seen, if we change the values of the augmenting function parameters α_g, β_g keeping the other model parameters f_0, s_f and $s_f - s_0^e$ at the same level. One can observe that such a change has almost no influence on the overall dynamics at $t = t_2$, see the inserts in Fig. 13. Indeed, while in the central part the permeability coefficients are almost two orders of magnitude different, the position of the front at $s = s_f$ is practically the same and the saturation level in the centre has only variations within approximately 15%. In what follows, we fix parameters of the augmented function at $\alpha_g = 16.5$ and $\beta_g = 1.65$ and scale parameter f_0 according to (32) using particular properties of the sand and the wetting liquid.

To understand the origin of the sharp transition observed in the saturation profiles, consider an intermediate asymptotic in the pendular regime of wetting, when $g(s) \approx 1$. Introducing new variable $\xi = (r - r_0)/\epsilon$, $\epsilon = const$ and $r_0 = const$, $\epsilon \ll 1$, and neglecting terms of the order of ϵ and relatively slow variations in the logarithmic term and in $\widehat{\kappa}_0(s)$, from (30)

$$\frac{\partial^2}{\partial\xi^2}\frac{1}{(s - s_0^e)^{1/2}} \approx 0.$$

Then

$$s \approx s_0 + \frac{1}{(W_0(r - r_0) + W_1)^2}. \tag{34}$$

As one can see, Fig. 14, the asymptotic behaviour matches very well the simulated saturation profiles at the point of the sharp transition and even in the tail region.

E. Universal scaling laws of the moving front propagation and the super-fast diffusion model

The distinctive shape of the saturation profiles suggests an explanation of the characteristic power laws of the front motion observed in the experiments. First of all, the total flux $\Pi_0(t)$ at the moving front $X_n(t)$ should be proportional to the moving front velocity, that is

$$\Pi_0(t) \propto X_n^{n-1}\frac{dX_n}{dt},$$

where index n designates here the dimension of the diffusion problem. At the same time, the asymptotic behaviour (34) suggests that parameter $W_0(t)$, Fig. 14 and the insert, should be inversely proportional to the length of the tail region $X_n(t) - r_0(t)$. Hence, when $X_n \gg r_0$, the total flux $\Pi_0(t)$ (since it is proportional to the gradient of saturation) should scale with $X_n(t)$ as $\Pi_0(t) \propto \frac{1}{X_n(t)}$. That is in the one-dimensional case

$$\frac{dX_1}{dt} \propto \frac{1}{X_1}.$$

This results in $X_1(t) \propto t^{1/2}$, which is the well-known Lucas-Washburn law for fluid motion in a circular capillary observed in our one-dimensional experiments. In a

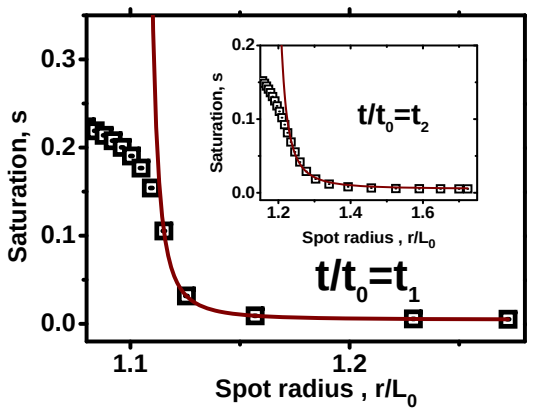

FIG. 14. Simulation of spreading in a three-dimensional spherically symmetric case using augmented superfast diffusion model (30) with initial distributions given by (33) at $\lambda_a = 0.2$ and $s_a = 0.5$. Saturation $s(r,t)$ as a function of the reduced spot radius r/L_0 at fixed values of $\alpha_g = 16.5$, $\beta_g = 1.65$, $f_0 = 1$, $s_f = 0.0052$ and $s_f - s_0^e = 0.0002$. A comparison between the asymptotic solution (34) (solid line, brown) and the numerical solution at $t = t_1 = 3 \times 10^{-6}$ shown by symbols, $W_0 \approx 287$. The insert shows a similar comparison, but at $t/t_0 = t_2 = 6 \times 10^{-5}$, $W_0 \approx 62$.

general case

$$X_n(t) \propto t^{1/(n+1)},$$

which in the three-dimensional case would give rise to $X_3 \propto t^{1/4}$ or $V(t) \propto X_3^3 \propto t^{0.75}$ - the power law observed in the three-dimensional experiments and simulations. We have also verified by numerical solution of the model that $X_2(t) \propto t^{1/3}$ in two-dimensional radially symmetric cases.

F. A comparison between numerical simulations and experimental results

Consider now a comparison between numerically found evolution curves of the moving front using (30) and the experimental observations. In all simulations we start from a profile with $\lambda_a = 0.3$ and $s_a = 0.4$, such that $L_0 = 3.24\,\mathrm{mm}$ at $V_D = 6\,\mathrm{mm}^3$. Consider spreading of TCP liquid drops ($V_D = 6\,\mathrm{mm}^3$) in $R = 0.26\,\mathrm{mm}$ sand, Fig. 15. In the simulations, we fixed the value of $s_f = 0.0061$ according to the experimental observations, Table I, and $s_f - s_0^e = 4.3 \times 10^{-4}$ according to the scaling (17) at $B_f = 29\,\mu\mathrm{m}^2$. The experimentally observed evolution curves $V(t)$ have been shifted by renormalising time $(t - t_s)/t_0$, $t_0 = L_0^2/D_f$, where an effective coefficient of diffusion D_f was the fitting parameter. The time t_s corresponds here to the actual time when the simulations started (about $30 - 90$ minutes of spreading), when the average saturation levels $\bar{s}$ observed in the experiments coincide with the initial average saturation levels in the simulations. As one can see the numerical solution is a good match to the observations giving $D_f = 7 \times 10^{-14}\,\mathrm{m}^2/\mathrm{s}$, while $D_0^e = (7 \pm 3.2) \times 10^{-14}\,\mathrm{m}^2/\mathrm{s}$ can be obtained assuming $\varepsilon_p = 0.15$ and $\theta_c = 30°$.

Now, in a similar way, we compare evolution of the moving front for TEHP and TBP liquid spots with numerical solutions, but with already fixed value of $\varepsilon_p = 0.15$. Those liquids have much smaller contact angle on a flat smooth/rough surface of quartz, $\theta_c \approx 10°/0°$ against $\theta_c \approx 30°/20°$ in the case of TCP liquids. Therefore, one can expect much higher permeability according to (8). In the comparison, we presume that for both TEHP and TBP the equilibrium saturation level is $s_f = 0.68\%$ ignoring the higher value of $s_f = 0.93\%$ found for TBP. This implies that the formation (and the thickness) of the liquid film on the rough surfaces of the sand grains, given similar wetting properties of both liquids, should be the same. One can observe, Fig. 15, very good agreement between numerical solutions and the experimental data, demonstrating the scaling of the propagation rates with the surface tension γ, liquid viscosity μ and contact angle θ_c through the permeability of the surface layer κ_0^1, (8), suggested by the diffusion coefficient D_0^e.

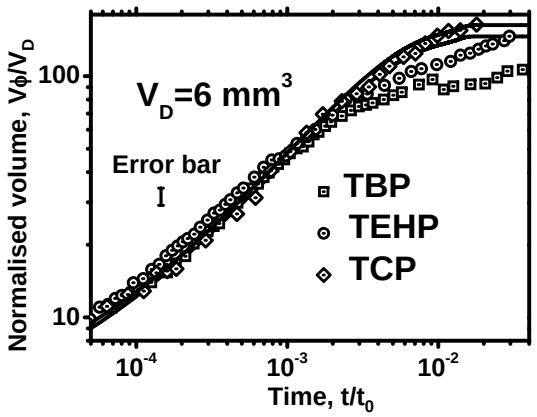

FIG. 15. Spreading of TCP, TEHP and TBP liquid drops ($V_D = 6\,\mathrm{mm}^3$) in $R = 0.25\,\mathrm{mm}$ sand ($R = 0.26\,\mathrm{mm}$ for TCP liquid). Comparison between experimental data and simulations using superfast diffusion model (30) with initial distribution of saturation given by (33). Normalised wet volume $V\phi/V_D$ (inverse average saturation $\bar{s}^{-1}$) as a function of the reduced time t/t_0, $t_0 = L_0^2/D_f$. Experimental data are shown by symbols and simulations are presented by the solid lines. Parameters of the simulations and the fitting are summarized in Table I.

Consider now how the average grain size affects the spreading in the pendular regime. We have done a series of experiments using TCP liquid drops ($V_D = 6\,\mathrm{mm}^3$) placed on sand beds with different average radius R, sets II, IV, V and VI, Table I. The results of a comparison between numerical solutions of the model and the data

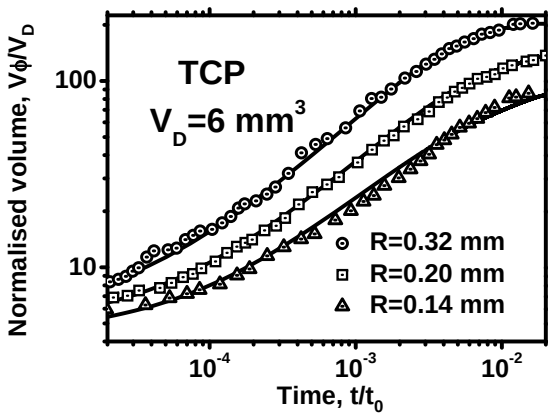

FIG. 16. Spreading TCP liquid drops ($V_D = 6\,\mathrm{mm}^3$) in sands with different grain radii $R = 0.14, 0.20$ and $0.32\,\mathrm{mm}$. Comparison between experimental data and simulations using superfast diffusion model model (30) with initial distribution of saturation given by (33). Normalised wet volume $V\phi/V_D$ (inverse average saturation $\bar{s}^{-1}$) as a function of the reduced time t/t_0, $t_0 = L_0^2/D_f$. Experimental data are shown by symbols and simulations are presented by solid lines. Parameters of the simulations and the fitting are summarized in Table I.

are shown in Figs. 15 and 16. In the simulations and in the comparison, we used scaling (17) with $B_f = 29\,\mu\mathrm{m}^2$ to estimate parameter $s_f - s_0^e$ and κ_0 at $\varepsilon_p = 0.15$. As one can see from the comparison, the model demonstrates the same trend as it was observed in the experiments. That is that the evolution is slower for smaller grain sizes R. In the model, this is a manifestation of the scaling of the parameter $s_f - s_0^e \propto R^{-2}$. The obtained values of the fitting parameter D_f were also in agreement with the values predicted by the theory D_0^e. The only exception is observed at the smallest value of R, which can be in principle mitigated by adjusting parameter $s_f - s_0^e$ within the uncertainty window. Alternatively, one can think that properties of the surface roughness, while not seen in the equilibrium distribution of the liquid, may be different for large and small grains. So that further improvement of the model would require, perhaps, more accurate characterizations of the sand particles and considerations of the flows within surface roughness, at the micro-scale.

Consider now, how the dynamics observed in three-dimensional spherically symmetric cases can be translated into one-dimensional geometry.

G. Dynamics of spreading in one-dimensional geometries

The liquid spreading was observed in the open channels, as is shown in Fig. 6, by placing a $V_D = 3\,\mathrm{mm}^3$ liquid drops of TCP, TEHP and TBP at one end of the groove. The numerical solutions were obtained by solving the augmented model (30) with $\alpha_g = 16.5$ and $\beta_g = 1.65$, as before, and with initial distributions given by

$$s(x,t)\mid_{t=0} = s_f + s_a \cos^{\lambda_a}(\pi x/2),\ \ 0 \le x \le 1 \qquad (35)$$

at $\lambda_a = 0.3$, $s_a = 0.2$. We use the same set of boundary conditions, together with $\partial s/\partial x = 0$ at $x = 0$ to reflect the absence of the flux at the end of the channel.

A comparison between the experimental data and the numerical solutions is shown in Fig. 17. In the comparison, we have taken all parameter values directly from the similar comparison in the three-dimensional geometry, Table I, with parameter L_0 defined according to the initial distribution (35)

$$\pi d_c^2 \phi \int_0^1 s(x,0)\,dx = 8 V_D L_0^{-1}.$$

We note that practically all parameter values in the comparison were fixed, we have only taken the liberty to vary L_0 within 1 mm to take into account the fact that the shape of the groove is hemispherical rather than cylindrical at the ends, Fig. 6, so that the one-dimensional model is an approximation.

As is seen, Fig. 17, the numerical solutions follow the propagation law observed in the experiments $X_1(t) \propto t^{0.5}$. Secondly, one can observe that the scaling suggested by the diffusion coefficient, $D_0 \propto \kappa_0^1 \frac{\gamma}{\mu}$, is well observed. Indeed, after re-scaling the time t/t_0, $t_0 = \frac{L_0^2}{D_f}$, the TCP, TBP and TEHP data collapsed into a single curve. Though the numerical solutions slightly overshoot the experimental curves, the overall comparison is looking very good considering that there were practically no fitting parameters involved.

H. Spreading in pre-wetted porous media

Even kiln-dried sands in open-chamber conditions would absorb some amount of the liquid present in the gas phase due to capillary condensation processes [34]. So we have conducted a series of spreading experiments in the presence of some background level s_r of the wetting liquid in the porous matrix to understand how the spreading dynamics would be affected by the pre-wet conditions. The pre-wetted sand samples were prepared by shaking and mixing a certain amount of the TEHP liquid with the sand in a closed container over a long period of time to ensure that the liquid is equally distributed in the sample. The experimental results of spreading of $V_D = 6\,\mathrm{mm}^3$ TEHP liquid drops in $R \approx 0.25\,\mathrm{mm}$ pre-wet sands are shown in Figs. 18 and 19 at different levels of s_r. The main question here is to understand if the mixing and shaking of the pre-wetted sand samples would have produced a similar liquid distribution on the grain surfaces to that obtained during the natural liquid spreading at similar saturation levels. Apparently, one might

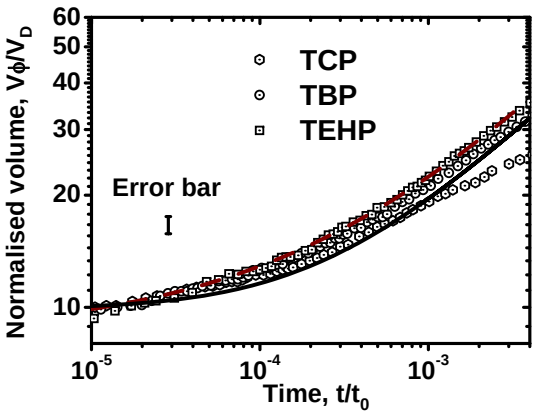

FIG. 17. Spreading TCP, TEHP and TBP liquid drops ($V_D = 3\,\mathrm{mm}^3$) in sands with $R = 0.25\,\mathrm{mm}$ in one-dimensional geometry. Comparison between experimental data and simulations using superfast diffusion model model (30) with initial distribution of saturation given by (35). Normalised wet volume $V\phi/V_D$ (inverse average saturation $\bar{s}^{-1}$) as a function of the reduced time t/t_0, $t_0 = L_0^2/D_f$. Experimental data are shown by symbols and simulation is presented by the solid line. Parameters of the simulations and the fitting are summarized in Table I. The dashed line (brown) is the fit $V\phi/V_D = A + B(t/t_0)^{0.5}$ at $A \approx 8.5$ and $B \approx 440$.

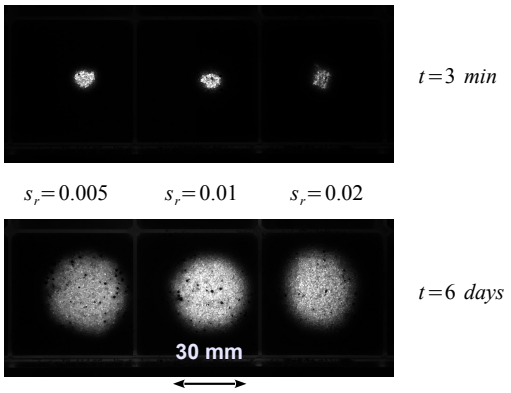

FIG. 18. Spreading of TEHP liquid drops ($V_D = 6\,\mathrm{mm}^3$) in pre-wetted sands with different background saturations levels $s_r = 0.5, 1$ and 2%. UV fluorescence wet spot areas taken at $t = 3\,\mathrm{min}$ and at $t = 6\,\mathrm{days}$ after the deposition of the drops on the sand bed.

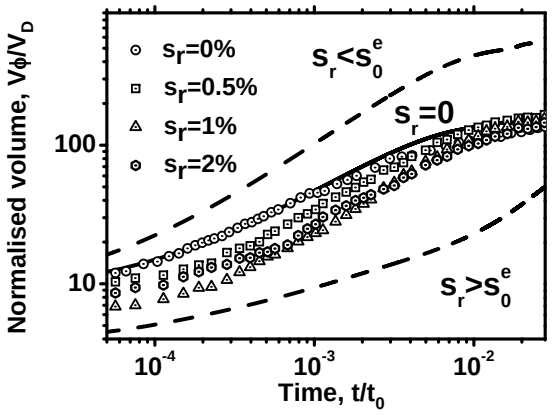

FIG. 19. Spreading of TEHP liquid drops ($V_D = 6\,\mathrm{mm}^3$) in pre-wetted sands with different background saturations levels $s_r = 0, 0.5, 1$ and 2%. Normalised wet volume $V\phi/V_D$ (inverse average saturation $\bar{s}^{-1}$) as a function of the reduced time t/t_0, $t_0 = L_0^2/D_f$. The experimental results are shown by symbols. The results of numerical simulations are shown by solid lines ($s_r = 0\%$) and by dashed lines $s_r = 1\%$ and $s_r = 0.5\%$.

expect that the distributions could be different due to the hysteresis effect commonly observed in porous media spreading processes [32, 34, 35]. For example, if some areas on the grain surfaces were inaccessible to the liquid flow at low saturation levels [11], then during shaking and mixing those areas might be wet. The assumption is in agreement with the analysis presented in [11] and our observations that the equilibrium value of $\alpha_R \approx 0.2$ after natural spreading is small. That is, during the natural spreading, large surface areas of the grains were left dry. This implies that the liquid content in equilibrium would depend on the way this equilibrium was achieved, and this seemed to be observed in our experiments, Figs. 18 and 19. Indeed, as is seen from the figures, the rate of the front evolution and the final size of the wet spot area were practically independent of the value of s_r, as if the sand was almost dry. One can observe some small effect of the background moisture presence, but as we will argue below, this was way too low.

Theoretically, if we presume for a while that our pre-wetted sands with some background level of saturation s_r have similar liquid morphology to that during the natural spreading, one should distinguish two cases. In the first case, when $s_r > s_0^e$, there should be liquid bridges present in the background porous material. In the second case, when $s_r < s_0^e$, the global network connection is broken. In the former case, the notion of the moving wetting front is absent as a matter of fact. Consider, as an example, again a spherically symmetric three-dimensional case, when initial liquid distribution at $t = 0$ is given by

$$s(r,0) = s_r + s_a \cos^{\lambda_a}(\pi r/2), \;\; 0 \le r \le 1 \qquad (36)$$

$$s(r,0) = s_r, \;\; 1 \le r \le r_a$$

and there is no flux at the end of the simulation domain at $r = r_a$, Fig. 20. Due to the nature of our numerical method, which is using moving meshes, the amount of the liquid is conserved in between any moving mesh points.

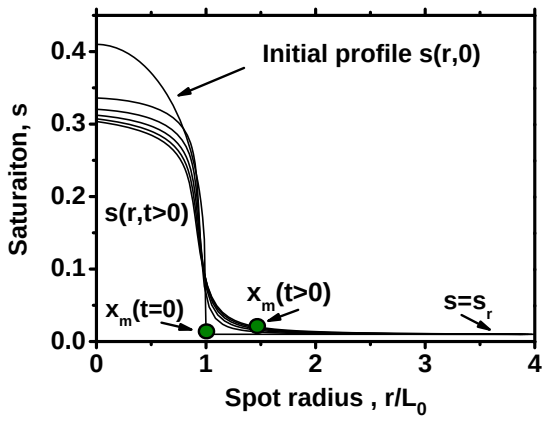

FIG. 20. Simulation of spreading of TEHP liquid drops ($V_D = 6\,\mathrm{mm}^3$) in pre-wetted sands with the background saturations level $s_r = 1\%$ using the augmented model (30) with initial conditions (36) at $s_a = 0.4$, $r_a = 4$ and $\lambda_a = 0.3$ with $s_0^e \approx 0.0068$.

Hence, one can easily follow the evolution of a benchmark point $x_m(t)$, as is shown in Fig. 20. The result at $s_r = 1\%$, shown in Fig. 19 in terms of the evolution of the volume contained within $0 \le r \le x_m$, indicates that while there is some initial plateau in the distribution of the saturation, as is observed in the experiments presented in the same figure, in general the evolution is much slower. One can conclude then that, while the initial plateau observed during the volume evolution at high average saturation values $\bar{s} \approx 20\%$ at both $s_r = 2\%$ and $s_r = 1\%$ indicates that the mechanism of spreading is sensitive to the background levels, see Fig. 19, to the large extent the spreading dynamics is still defined by the front capillary pressure generated on the scale of surface roughness. One can also conclude that the liquid morphology of that background liquid distribution seemed to be different from the liquid morphology observed at these saturation levels during the natural spreading.

In the second case, $s_r < s_0^e$, one needs to modify the original model to include the presence of some background saturation level. Using conservation of the liquid in the domain Ω with a front $\partial\Omega(t)$ moving into the area with background saturation s_r and the transport Reynolds theorem

$$\frac{d}{dt}\int_{\Omega(t)} s\, d^3x = \int_{\Omega(t)} \left(\frac{\partial s}{\partial t} + \nabla\cdot(s\mathbf{v})\right) d^3x =$$

$$= \int_{\partial\Omega(t)} (\mathbf{v}\cdot\mathbf{n})\, s_r\, dS,$$

where $\mathbf{n}$ is the normal vector to $\partial\Omega$.

Transforming the surface integral into the volume integral

$$\int_{\Omega(t)} \left(\frac{\partial s}{\partial t} + \nabla\cdot((s - s_r)\mathbf{v})\right) d^3x = 0.$$

This implies that an equivalent moving boundary-value non-linear diffusion problem of transport in pre-wetted sands can be formulated in terms of a function $\varphi = s - s_r$

$$\frac{\partial\varphi}{\partial t} = \nabla\left\{\frac{\widehat{\kappa_0}(\varphi)\,\widehat{g}\,(\varphi)\nabla\varphi}{|\ln(\varphi-\varphi_0)|(\varphi-\varphi_0)^{3/2}}\right\}, \qquad (37)$$

$$\varphi_0 = s_0^e - s_r$$

with the boundary conditions

$$\varphi|_{\partial\Omega} = s_f - s_r$$

and

$$v_n|_{\partial\Omega} = -\frac{\widehat{\kappa_0}(\varphi)\,\widehat{g}\,(\mathbf{n}\cdot\nabla)\varphi}{(s_f - s_r)|\ln(s_f - s_0^e)|(s_f - s_0^e)^{3/2}}. \qquad (38)$$

One can see that in general due to a smaller factor at the moving front $s_f - s_r$ (instead of just s_f), the front motion is expected to proceed with much higher velocity. This is understandable, since one requires lesser amount of the liquid to move the front by an infinitesimal value Δx within a time interval Δt, and this is exactly what was observed in the numerical solutions of (37)-(38) at the parameters of set VIII, Table I, and initial distribution (33) at $\lambda_a = 0.3$ and $s_a = 0.4$, Fig. 19. As one can see, the propagation of the front is indeed much faster than that at $s_r = 0$ shown in the same figure. One might expect that the value of the parameter $s_f - s_0^e$ would be larger in this case, since in the pre-wetted sand the small length scales of the surface roughness may not be available. This might reduce the capillary pressure at the moving and slow down the propagation rate. But, we have checked that even increasing the value of $s_f - s_0^e$ by three times was insufficient to match the slower propagation observed in the experiment. This again indicates that the liquid morphology is different at $s_r = 0.5\%$ than one would anticipate. Basically, the wetting process is unaffected by the presence of small background levels. In a way, this result is in accord with the characteristic values of the coefficient $\alpha_R \approx 0.2$ obtained in the comparison with experimental data. This indicates, that only a limited part of the surface area of the grains is fully participating in the liquid transport in the system. We note, that given the length scale of the liquid films involved in the transportation in the pendular regime, it is unlikely to have stochastic enhancement of the dye transport in the wet porous matrix [36]. These are very interesting results, which definitely require further, specific studies.

CONCLUSIONS

In our previous study we established that:

- The process of spreading can be described by a special type of non-linear diffusion process, where the driving force is the capillary pressure at the moving front generated by the particle surface roughness and the coefficient of diffusion has a characteristic singular form $D(s) \propto (s - s_0^e)^{-3/2}$. The resulting mathematical model belongs to a class known as super-fast diffusion equation, and the so-suggested scaling with viscosity and surface tension is as expected for capillary flows, $D \propto \gamma/\mu$.

- Motion of the wetting front $X_3(t)$ in a three-dimensional spherically symmetric domain (when the wetted volume has a shape of the hemisphere) exhibits universal scaling behaviour with time t, such that $X_3(t) \propto t^{1/4}$, ultimately going to stand-still at finite saturation levels $s_0 \approx 0.6\%$. This behaviour led us to a conjecture, confirmed in numerical simulations of the superfast diffusion model, that in general, depending on the geometry, basically on its dimension n, $X_n(t) \propto t^{1/(n+1)}$, which may be used in practical applications to analyse such kind of spreading processes.

In the work reported here, with the help of a new set of experiments, we have delved deeper into the theoretical formulation aiming to refine the modelling of relevant permeability and include the funicular regime, so as to supply improved initial conditions for the super-fast regime. The experiments were carried out with a set of low-dispersed (with small deviations of the grain radius R from its average value), well characterized sands, using different geometric set-ups and regimes of spreading (one- and three-dimensional symmetric regimes). The new results can be summarized as follows:

1. The motion of the liquid wetting front $X_n(t)$ in geometrically different set-ups and regimes of liquid spreading indeed follows the universal scaling law $X_n(t) \propto t^{1/n+1}$, with n being solely defined by the dimension of the moving front diffusion problem. As it was shown by the numerical analysis, the augmented superfast diffusion model (30) clearly demonstrates this universal behaviour, which may be used in the practical applications for the analysis of spreading at low saturation levels. Analysis of the mathematical model has revealed that this behaviour is manifestation of the specific shape of the saturation profile (a Mexican hat), predicted by the model, with a distinctive tail at almost equilibrium saturation levels $s \approx s_f$. In the one-dimensional case, when spreading is confined within long, open channels, the advancing-front motion conforms to the well-known Lucas-Washburn law $X_1(t) \propto t^{1/2}$ for a single capillary.

2. The overall evolution of the wetted volume is predominantly defined by the diffusion rates in the tail region, that is by the processes described by the super-fast diffusion model. On the other hand, the standard diffusion mechanisms, commonly applied for the analysis of spreading in the funicular regime of wetting, only smooth out the distribution profile at higher levels of saturation, usually found in its central part. Thus, the funicular and the pendular regimes are found to simply operate simultaneously but in different locations.

3. Experimental data obtained using liquids of different viscosities and wettabilities confirm our previous finding that the spreading dynamics of different liquids obeys the scaling law when the driving force is the capillary pressure, and the coefficient of diffusion $D \propto \gamma/\mu$, as is depicted by our superfast diffusion model. Further, we have been able to identify the scaling behaviour of diffusion with the wettability of the liquid-solid combinations involved, that is with the contact angle θ_c. As it might be expected, the diffusion rate is found to be smaller for larger contact angles. This effect is directly related with the available amount of the surface roughness groove filling, which diminishes as the contact angle increases.

4. A set of experiments using low-dispersed sand samples with different distributions of the grain sizes has allowed to obtain more accurate estimates of the main non-dimensional parameters of the model, such that only one adjusting parameter ε_p was left incorporating nothing but specific microscopic properties of the surface roughness. Spreading dynamics observed in sands with different grain size distributions was found to be slightly counter-intuitive. The spreading was slower when the grain size reduces, while the effective surface area per unit volume $S_T \propto 1/R$ (and hence the effective free surface energy) increases. This behaviour is in accord with the mathematical model and is manifestation of the scaling of the main non-dimensional model parameter $s_f - s_0^e \propto 1/R^2$, which is in fact the inverse of the capillary front pressure, the main driving force of the process.

5. Analysis of spreading in pre-wet sands with a small background level of saturation $s_r \approx 1 - 2\%$ have shown, that the distributions of the same amount of a liquid are different after natural spreading and mechanical mixing procedures. If a small background saturation level was achieved by a mechanical mixing process, it does not change dramatically the dynamics of spreading predicted by the superfast diffusion model.

6. While the dynamics of liquid spreading was found to depend on the liquid and porous media properties, the equilibrium thickness of the liquid film on

the surface of grains was solely defined by the surface roughness, at least for the well-wetting liquid-solid combinations used in our study. Such universal behaviour allows to predict one of the main parameters of the model $s_f \approx s_0$ with sufficient accuracy only on the basis of the effective surface area $S_T \propto 1/R$, porosity ϕ and the average amplitude of the surface roughness δ_R.

One can then finally conclude that on the basis of comparison with experimental data the augmented superfast non-linear diffusion model (30) provides adequate description of liquid transport at low saturation levels, which therefore can be used in practical applications.

[1] Herminghaus, S., Dynamics of wet granular matter *Adv. Phys.* **54**, 221, (2005)

[2] Scheel, M.; Seemann, R.; Brinkmann, M.; Michiel, M.D.I.; Sheppard, A.; Breidenbach, B. and Herminghaus, S., Morphological clues to wet granular pile stability *Nature Mater.* **7**, 189, (2008)

[3] Scheel, M.; Seemann, R.; Brinkmann, M.; Michiel, M.D.I.; Sheppard, A. and Herminghaus, S., Liquid distribution and cohesion in wet granular assemblies beyond the capillary bridge regime *J. Phys. Condens. Matter* **20**, 494236, (2008)

[4] Melnikov, K.; Wittel, F.K. and Herrmann, H.J., Micromechanical failure analysis of wet granular matter *Acta Geotech.* **11**, 539–548, (2016)

[5] Orr, F.M.; Scriven, L.E. and Rivas, A.P., Pendular rings between solids: meniscus properties and capillary force *J. Fluid Mech.* **67**, 723-742, (1975)

[6] Willett, C.D.; Adams, M.J.; Johnson, S.A. and Seville, J.P.K., Capillary Bridges between Two Spherical Bodies *Langmuir* **16**, 9396–9405, (2000)

[7] Lukyanov, A.V.; Sushchikh, M.M.; Baines, M.J. and Theofanous, T.G., Superfast Nonlinear Diffusion: Capillary Transport in Particulate Porous Media *Phys. Rev. Lett.* **109**, 214501, (2012)

[8] Halsey, T.C. and Levine, A.J., How Sandcastles Fall *Phys. Rev. Lett.* **80**, 3141-3144, (1998)

[9] Alshibli, K.A. and Alsaleh, M.I., Characterizing Surface Roughness and Shape of Sands Using Digital Microscopy *J. Comput. Civil Eng.* **18**, 36-45, (2004)

[10] Tokunaga, T.K. and Wan, J., Water film flow along fracture surfaces of porous rock *Water Resour. Res.* **33**, 1287–1295, (1997)

[11] Or, D. and Tuller, M., Flow in unsaturated fractured porous media: Hydraulic conductivity of rough surfaces *Water Resour. Res.* **36**, 1165–1177, (2000)

[12] Tuller, M. and Or, D., Water films and scaling of soil characteristic curves at low water contents *Water Resour. Res.* **41**, 09403, (2005)

[13] de Gennes, P.G., Partial Filling of a Fractal Structure by a Wetting Fluid. In *Physics of Disordered Materials* edited by D. Adler, E. Fritzsche and S.R. Ovshirisky (Plenum Press, New York, 1985, pp. 227-241).

[14] Novy, R.A.; Toledo, P.G.; Davis, H.T. and Scriven, L.E., Capillary Dispersion in Porous Media at Low Wetting Phase Saturations *Chem. Eng. Sci.* **44**, 1785–1797, (1989)

[15] Toledo, P.G.; Davis, H.T. and Scriven, L.E., Capillary Hyperdispersion of Wetting Liquids in Fractal Porous Media *Transport Porous Med.* **10**, 81–94, (1993)

[16] Bacri, J.C.; Leygnac, C. and Salin, D., Evidence of capillary hyperdiffusion in two-phase fluid flows *Journal de Physique Lettres* **46**, 467–473, (1985)

[17] Skene, W.G. and Krzymien, M.E., Vapor pressure of TBP *J. Chem. Eng. Data* **40**, 394–397, (1995)

[18] Patnaik, P., *Handbook of Environmental Analysis: Chemical Pollutants in Air, Water, Soil, and Solid Wastes* (Second Edition, Taylor & Francis 2010)

[19] Romero, L.A. and Yost, F.G., Flow in an open channel capillary *J. Fluid Mech.* **322**, 109–129, (1996)

[20] Rye, R.R.; Yost, F.G. and O'Toole, E.J., Capillary flow in irregular surface grooves *Langmuir* **14**, 3937, (1998)

[21] Ransohoff, T.C. and Radke, C.J., Laminar flow of a wetting liquid along the corners of a predominantly gas-occupied noncircular pore *J. Colloid Interface Sci.* **121**, 392–401, (1988)

[22] Concus, P. and Finn, R., On the Behavior of a Capillary Surface in a Wedge *PNAS* **63**, 292-299, (1969)

[23] Matyka, M.; Khalili, A. and Koza, Z., Tortuosity-porosity relation in porous media flow *Phys. Rev. E* **78**, 026306, (2008)

[24] Whitaker, S., Advances in Theory of Fluid Motion in Porous Media *Ind. Eng. Chem.* **61**, 14–28, (1969)

[25] Vazquez, J.L., *Smoothing and Decay Estimates for Nonlinear Diffusion EquationsEquations of Porous Medium Type* (Oxford University Press, New York, 2006)

[26] Aronson, D.G., The porous-medium equation *Lecture Notes in Mathematics* **1224**, 1–46, (1986)

[27] Barenblatt, G.I., *Scaling* (Cambridge University Press, 2003)

[28] Vazquez, J.L., *The Porous Medium Equation: Mathematical Theory* (Oxford University Press, 2006)

[29] Vazquez, J.L., Barenblatt solutions and asymptotic behaviour for a nonlinear fractional heat equation of porous medium type *J. Eur. Math. Soc.* **16**, 769–803, (2014)

[30] Mackay, D. and van Wesenbeeck, I., Correlation of Chemical Evaporation Rate with Vapor Pressure *Environ. Sci. Technol.* **48**, 10259–10263, (2014)

[31] Koorevaar, O.; Menelik, G. and Dirksen, C., *Elements of soil physics* (Elsevier, Amsterdam, 1983)

[32] Leverett, M.C., Capillary Behavior in Porous Solids *Transaction of AIME* **142**, 341–358, (1941)

[33] Gummerson R.J.; Hall, C.; Hoff, W.D.; Hawkes, R.; Holland, G.N. and Moore, W.S., Unsaturated Water-flow within Porous Materials Observed by NMR Imaging *Nature* **281**, 56–57, (1979)

[34] Kierlik, E.; Monson, P.A.; Rosinberg, M.L.; Sarkisov, L. and Tarjus, G., Capillary Condensation in Disordered Porous Materials: Hysteresis versus Equilibrium Behavior *Phys. Rev. Lett.* **87**, 055701, (2001)

[35] Mualem, Y., A conceptual model of hysteresis *Water Resour. Res.* **10**, 514–520, (1974)

[36] Kulasiri, D. and Wynand Verwoerd, W., *Stochastic Dynamics. Modeling Solute Transport in Porous Media. Series in Applied Mathematics and Mechanics* **44**, (North-Holland, 2002)

[37] Lee, T.E.; Baines, M.J. and Langdon, S., A Finite Difference Moving Mesh Method based on Conservation for Moving Boundary Problems *J. Comput. Appl. Math.* **288**, 1–17, (2015)

[38] Baines, M.J., *A Positivity- and Monotonicity-preserving Moving-mesh Finite Difference Scheme based on Local Conservation* Mathematics Report 1/17, (2017) Department of Mathematics and Statistics, University of Reading, UK, http://www.reading.ac.uk/web/files/maths/semi-implicit.pdf

APPENDIX: NUMERICAL MOVING MESH METHOD.

The numerical technique used to solve the partial differential equations in this study is a moving mesh method driven by conservation, similar to that presented in [37] and described in [38]. A nodal velocity v is constructed from a combination of a non-linear diffusion equation, for example the 3-D radially symmetric nonlinear diffusion equation

$$\frac{\partial s}{\partial t} = \frac{1}{r^2}\frac{\partial}{\partial r}\left(r^2 D(s)\frac{\partial s}{\partial r}\right),$$

and the conservation law

$$\frac{\partial s}{\partial t} + \frac{1}{r^2}\frac{\partial}{\partial r}\left(r^2 s v\right) = 0, \tag{39}$$

yielding the velocity formula

$$v(r,t) = -\frac{D(s)}{s}\frac{\partial s}{\partial r} \tag{40}$$

where $v(0,t) = 0$. An equation for $\mathrm{d}s/\mathrm{d}t$ following the motion is then

$$\frac{\mathrm{d}s}{\mathrm{d}t} = \frac{\partial s}{\partial t} + v(r,t)\frac{\partial s}{\partial r} = -\frac{1}{r^2}\frac{\partial}{\partial r}\left(r^2 s v\right) + v(r,t)\frac{\partial s}{\partial r}$$

$$= -s\frac{1}{r^2}\frac{\partial}{\partial r}\left(r^2 v\right) = s\frac{1}{r^2}\frac{\partial}{\partial r}\left(r^2\frac{D(s)}{s}\frac{\partial s}{\partial r}\right) \tag{41}$$

Introducing moving nodes $\widehat{r}_i(t)$ and corresponding saturation values $\widehat{s}_i(t)$, $(i = 1, \ldots, N)$, an approximation to (40) is

$$v^n_{i+1/2} = -\frac{D(\widehat{s}^n_{i+1/2})}{\widehat{s}^n_{i+1/2}}\frac{\widehat{s}^n_{i+1} - \widehat{s}^n_i}{\widehat{r}^n_{i+1} - \widehat{r}^n_i} \tag{42}$$

The system (41) is approximated by the first-order-in-time semi-implicit scheme

$$\frac{\widehat{s}^{n+1}_i - \widehat{s}^n_i}{\Delta t} = \frac{\widehat{s}^n_i}{(\widehat{r}^n_{i+1/2} - \widehat{r}^n_{i-1/2})(\widehat{r}^n_i)^2}$$
$$\left\{ (\widehat{r}^n_{i+1/2})^2\frac{D(\widehat{s}^n)}{\widehat{s}^n}\bigg|_{i+1/2}\frac{(\widehat{s}^{n+1}_{i+1} - \widehat{s}^{n+1}_i)}{(\widehat{r}^n_{i+1} - \widehat{r}^n_i)}\right.$$

$$\left. - (\widehat{r}^n_{i-1/2})^2\frac{D(\widehat{s}^n)}{\widehat{s}^n}\bigg|_{i-1/2}\frac{(\widehat{s}^{n+1}_i - \widehat{s}^{n+1}_{i-1})}{(\widehat{r}^n_i - \widehat{r}^n_{i-1})}\right\} \tag{43}$$

$(i = 1, \ldots, N-1)$ where Δt is the time step, which has the property that no new local extrema in $\widehat{s}_i$ are created in the interior of the domain in a time step, thereby preserving positivity of $\widehat{s}_i$ and avoiding oscillations. This allows arbitrarily large numbers of nodes without Δt being restricted by stability conditions.

The scheme (43) can be written in the matrix form

$$B\underline{\widehat{s}}^{n+1} = \underline{\widehat{s}}^n \tag{44}$$

where $\underline{\widehat{s}}^{n+1} = \{\widehat{s}^{n+1}_i\}$, $\underline{\widehat{s}}^n = \{\widehat{s}^n_i\}$, and B is a tridiagonal matrix modified to take into account the boundary condition $\widehat{s}_N = s_f$ and the continuity condition $\partial s/\partial r = 0$ at $r = 0$.

Once the $\widehat{s}^{n+1}_i$ have been obtained the mesh nodes $\widehat{r}^{n+1}_i$ can be found from the Lagrangian form of the conservation principle (39), i.e.

$$\int \widehat{s}(r,t) r^2 \mathrm{d}r \text{ is constant in time,} \tag{45}$$

valid when $s(r,t) > 0$.

A discretisation of (45) is

$$\{(\widehat{r}^{n+1}_{i+1})^3\widehat{s}^{n+1}_{i+1} - (\widehat{r}^{n+1}_i)^3\widehat{s}^{n+1}_i\} = \text{ its initial value} \tag{46}$$

$(i = 2, \ldots, N)$, yielding $\widehat{r}^{n+1}_i$ by recursion over i, given $\widehat{r}^{n+1}_0 = 0$. Since the s^{n+1}_i are positive the recursion process ensures that the nodes remain ordered.

To summarise the algorithm, given the r^n_i and s^n_i values at time step n,

- approximate the $v^n_{i+1/2}$ from (42)
- determine the $\widehat{s}^{n+1}_i$ from (43), equivalently (44)
- recover the r^{n+1}_i from (46).